

Measurement of Something

by

Kiyotaka Akabori

Submitted in partial fulfillment of the
requirements for the degree of

Doctor of Philosophy

at

Carnegie Mellon University

Department of Physics

Pittsburgh, Pennsylvania

Advised by Professor John F. Nagle
and Professor Stephanie Tristram-Nagle

June 25, 2014

Contents

1	Introduction	1
2	Materials and Methods	3
2.1	X-ray optics	3
2.2	Hydration Chamber	3
2.3	Sample Preparation	4
2.3.1	Stock Solutions	4
2.3.2	Thin Film Samples	4
2.4	CCD detector	5
3	Structural Perturbation of Lipid Bilayers Due to Tat Peptide	6
3.1	Introduction	6
3.2	Materials and Methods	9
3.2.1	Volume Measurements	9
3.2.2	Analysis of Diffuse Scattering	11
3.2.3	Modeling the Bilayer Structure	17
3.2.4	Molecular Dynamics Simulation	23
3.3	Analysis of Molecular Dynamics Simulation Data	26
3.3.1	SIMtoEXP program	26
3.3.2	Local Thinning of Membranes	26
3.3.3	Lateral Decay Length of Membrane Thinning	28
3.4	Results	30
3.4.1	Bending and Bulk Modulus	30
3.4.2	Volume results	32
3.4.3	Electron Density Profile Modeling	33
3.4.4	Hard Wall Constrain Fits	43

3.4.5	Summary of Electron Density Profile Modeling	44
3.4.6	Molecular Dynamics Simulations	46
3.5	Discussion	55
3.6	Conclusion	58
4	Ripple Phase	60
4.1	Introduction	60
4.2	Materials and Methods	62
4.2.1	Sample Preparation	62
4.2.2	Instrumental Resolution	63
4.2.3	Low Angle X-ray Scattering Experiment	65
4.2.4	Near Grazing Incidence Wide Angle X-ray Scattering Experiment	67
4.2.5	Transmission Wide Angle X-ray Scattering Experiment	71
4.3	LAXS analysis	78
4.3.1	Lattice Structure	78
4.3.2	Sample q-space	79
4.3.3	Lorentz Correction	81
4.3.4	Absorption Correction for LAXS	86
4.3.5	Absorption Correction for WAXS	90
4.3.6	Effect of mosaic spread	90
4.4	Model	90
4.4.1	Contour Part of the Form Factor	90
4.4.2	Transbilayer Part of the Form Factor	91
4.5	Results	92
4.5.1	Data and Electron Density Profile	92
4.5.2	Near Grazing Incidence Wide Angle X-ray Scattering (NGI- WAXS)	94
4.5.3	Transmission WAXS	94
4.6	Discussion	98
4.7	Conclusion	98
	Appendices	99
A	Tat	100
A.1	Analysis of Fixed Angle Data using NFIT	100

A.1.1	Theory	100
A.1.2	Results	100
A.2	Mosaic Spread for NFIT analysis	100
A.2.1	Mosaic Spread: Calculation	100
A.2.2	Mosaic Spread: Experiment	104
A.2.3	NFIT	108
A.2.4	Results	109
A.3	Domain Size Distribution: Gaussian and Exponential	109
A.4	Hard Wall Constraints in SDP	109
A.5	Some More Details of Tat Stuff	109
B	Ripple Phase	110
B.1	Derivation of the contour part of the form factor	110
B.2	Rotation of a Two-Dimensional Function	112
B.3	Derivation of the transbilayer part of the form factor in the 2G hybrid model	113
B.4	Correction due to refractive index	115

List of Tables

3.1	Some Amino Acids Data	10
3.2	Number of electrons per lipid and volume per lipid.	22
3.3	Some structural parameters for each component. n_i^e is the number of electrons and ρ_i is the average electron density.	22
3.4	Tat basic structural parameters. The notations are the same as in Table 3.3. $x_{\text{Tat}} = \text{Tat}/(\text{Tat}+\text{Lipid})$	22
3.5	Volume results at 37 °C	33
3.6	Fitting Results for DOPC membranes for the THG (Tat in headgroup) model. $z_{\text{PC}} - z_{\text{CG}} = 3.1 \text{ \AA}$ and $z_{\text{CG}} - z_{\text{HC}} = 1.3 \text{ \AA}$ in all fits.	34
3.7	Fitting Results for DOPC:DOPE (3:1) membranes for the THG model. $z_{\text{PC}} - z_{\text{CG}} = 3.1 \text{ \AA}$ and $z_{\text{CG}} - z_{\text{HC}} = 1.3 \text{ \AA}$ in all fits.	37
3.8	(Numbers are wrong) Fitting Results for DOPC:DOPE (1:1) membranes for the THG model. $\Delta z_1 = z_{\text{PC}} - z_{\text{CG}}$ and $\Delta z_2 = z_{\text{CG}} - z_{\text{HC}}$	37
3.9	Fitting Results of the bound THG model for DOPC membranes. $\Delta z_1 = z_{\text{PC}} - z_{\text{CG}}$ and $\Delta z_2 = z_{\text{CG}} - z_{\text{HC}}$	44
3.10	Comparison of the simulated form factors to the experimental form factors.	51
3.11	Summary of simulation results. $\langle D_{\text{PP}} \rangle$, phosphorus-phosphorus distance averaged over all lipids; D_{PP} , Tat-perturbed phosphorus atoms; x , thickness away from Tat; Δt , $\langle D_{\text{PP}}^{\text{DOPC}} \rangle - D_{\text{PP}}$; H_{Tat} , Tat height; R_{Tat} , radius of Tat cylinder; R_2 , radius of the calculated in-plane Tat-perturbed region; R_3 , effective radius of the simulation box.	52
3.12	Summary of weighted average results. The caption is the same as Table 3.11.	52

4.1	Lattice constants for DMPC at $T = 18.0$ °C reported by Wack and Webb [1]. The data collected and analyzed in this thesis are colored blue.	62
4.2	Definitions of Z_{CH_2} and Z_{W}	92
4.3	Observed intensity	93

List of Figures

3.1	LAXS of DOPC:DOPE (1:1) with $x_{\text{Tat}} = 0.034$ at 37 °C. White lobes of diffuse scattering intensity have large grey numbers, while lamellar orders and beam are shown to the left of the molybdenum beam attenuator (short, dark rectangle). q_z and q_r are the cylindrical coordinates of the sample q -space, where q_z -axis is along the bilayer normal and q_r -axis is along the in-plane direction. The lamellar repeat spacing was $D = 66.2 \text{ \AA}$	12
3.2	Schematic of an oriented stack of lipid bilayers. Thick green curves represent an instance of thermally fluctuating bilayers. The dashed lines show the thermally averaged positions $z = nD$ of the centers of each bilayer and $u_n(x, y)$ gives the instantaneous deviation from the average. Each bilayer extends in the $\mathbf{r} = (x, y)$ plane.	13
3.3	Expanded view of a fluctuating bilayer. Along the two black solid lines, the electron density profile is identical in an incompressible bilayer. Along the dashed line, the bilayer appears thicker by a factor $1/\cos \alpha$. This apparent thickness variation along the z direction is corrected by the undulation correction.	14
3.4	Schematic of DOPC showing each lipid component. The dash lines show where the lipid is divided into different components. The lipid headgroup is divided into two components, phosphate-choline (PC) and carbonyl-glycerol (CG). The hydrocarbon chain region is also divided into two components, methylene+methine (CH_2+CH) and terminal methyl groups (CH_3).	18
3.5	A model electron density profile for DOPC with Tat.	19

3.6	Our simple model to extract the local bilayer thickness from simulation trajectories. Tat is modeled as a cylinder with its height H_{Tat} and radius R_{Tat} . The local thickness is defined as $D'_{\text{phos-phos}}$. The thickness of the unperturbed DOPC bilayer is $D_{\text{phos-phos}}$. Blue highlighted lipids fall within the imaginary cylinder extended from the Tat. Unperturbed lipids are highlighted in green.	27
3.7	Simple model of the lateral decay of the membrane thickness perturbation due to Tat.	29
3.8	Bilayer bending modulus, K_c , vs. Tat mole fraction x_{Tat} . D -spacings for DOPC/Tat mixtures varied from 64 to 68 Å, for DOPC/DOPE/Tat mixtures from 64 to 69 Å, for DOPC/DOPS/Tat (3:1) mixtures from 57 Å to 100 Å (pure DOPS was unbound), and for nuclear mimic/Tat mixtures from unbound (nuclear mimic) to 64 Å. Estimated uncertainty in all values is about ± 2	31
3.9	Form factors of lipid mixtures (arbitrarily scaled and vertically displaced) with increasing Tat mole fractions x_{Tat} indicated on figure legends. Lipid mixtures: A. DOPC B. DOPC/DOPE (3:1) C. DOPC/DOPE (1:1) D. DOPC/DOPS (3:1) E. Nuclear mimic. The entire q_z range is shown in C, while others show partial ranges. Solid vertical lines indicate the q_z values where the form factors equal zero between the lobes of diffuse data.	32
3.10	The best fits to DOPC form factors (left) and the corresponding electron density profiles (right) with $x_{\text{Tat}} = 0, 0.016, 0.034$, and 0.059 (from top to bottom).	35
3.11	The best fits to DOPC:DOPE (3:1) form factors (left) and the corresponding electron density profiles (right) with $x_{\text{Tat}} = 0, 0.016, 0.034$, and 0.059 (from top to bottom).	36
3.12	The best fits to DOPC:DOPE (1:1) form factors (left) and the corresponding electron density profiles (right) with $x_{\text{Tat}} = 0, 0.016, 0.034$, and 0.059 (from top to bottom).	38
3.13	Modeling results for absolute electron density profiles and for the Tat location as a function of distance z along the bilayer normal. A. DOPC B. DOPC:DOPE (3:1), and C. DOPC:DOPE (1:1).	39

3.14	A. Bilayer thickness, D_{PP} ; B. Bilayer thickness, D_{HH} ; C. Area/lipid, A_L ; D. Twice the Tat location, $2z_{Tat}$: all plotted vs. Tat mole fraction x_{Tat} . Error bars are standard deviations from imposing Tat Gaussian widths, $\sigma_{Tat} = 2.5, 3.0$ or 3.5 Å. Inverted blue triangles connected with dotted line are results from MD simulations, averaging the best fits to the X-ray data for each parameter, with standard deviations shown. .	41
3.15	χ^2 as a function of z_{Tat} for DOPC, DOPC:DOPE (3:1), and DOPC:DOPE (1:1) (from left to right) with $x_{Tat} = 0.016, 0.034$, and 0.059 (from top to bottom). $\sigma_{Tat} = 3.0$. The THG model (black squares) and the THC model (red circles).	42
3.16	χ^2 as a function of z_{Tat} for DOPC with $x_{Tat} = 0.016, 0.034$, and 0.059 (from top to bottom). $\sigma_{Tat} = 3.0$. The bound THG model was used. .	45
3.17	DPP graph with bound fits	46
3.18	DHH graph with bound fits	46
3.19	AL graph with bound fits	46
3.20	z_{Tat} graph with bound fits	46
3.21	MD simulated form factors for DOPC at $A_L = 68$ Å ² (blue solid line), 70 Å ² (red solid line), and 72 Å ² (green solid line) compared to the experimental form factor (open circles) scaled vertically to best match the form factor for 70 Å ²	47
3.22	The simulated, symmetrized electron density profile for DOPC at $A_L = 70$ Å ² as a function of the distance away from the bilayer center. Each component profile is labeled with its name: PC (phosphate-choline), CG (carbonyl-glycerol), CH ₂ +CH (methylene-methine combination), CH ₃ (terminal methyl). The sum of all the components is labeled as total.	48
3.23	MD simulated form factors for DOPC with $x_{Tat} = 0.015$ at $A_L = 72$ Å ² (top) and 74 Å ² (bottom), with $z_{Tat} = 18$ Å (red solid lines), 16 Å (green solid lines), and 14 Å (blue solid lines) compared to the experimental form factor (open circles) scaled vertically to best match the form factor for $z_{Tat} = 18$ Å.	49

3.24	MD simulated form factors for DOPC with $x_{\text{Tat}} = 0.030$ at $A_L = 74 \text{ \AA}^2$ (top) and 76 \AA^2 (bottom), with $z_{\text{Tat}} = 18 \text{ \AA}$ (red solid lines), 16 \AA (green solid lines), and 14 \AA (blue solid lines) compared to the experimental form factor (open circles) scaled vertically to best match the form factor for $z_{\text{Tat}} = 18 \text{ \AA}$	50
3.25	Electron density profiles of guanidinium groups from the four best matched simulations for DOPC with $x_{\text{Tat}} = 0.015$ (one Tat on each leaflet). Tat on the lower and upper leaflets are shown on the left and right plots, respectively.	53
3.26	MD simulated form factors (red solid lines in A and C) of Tat/(DOPC+Tat), $x_{\text{Tat}}=0.030$, with Tat fixed at $z_{\text{Tat}}= 18 \text{ \AA}$ (panel A) and 5 \AA (panel C) from the bilayer center compared to experimental form factors (open circles) scaled vertically to provide the best fit to the simulations. Corresponding snapshots are shown in Panels B and D in which the lipid chains are represented as grey sticks on a white background, Tats are yellow, phosphate groups are red and water is blue.	54
3.27	Location of Tat in DOPC bilayer. Tat is represented as a cylinder, z is the distance from the bilayer center, and R is the in-plane distance from the center of Tat. The average z of the lipid phosphates as a function of R and the arginine guanidiniums are shown in red and blue, respectively.	55
4.1	Lattice structure of the asymmetric ripple phase. Unit cells are shown in dash lines. Center of bilayers are shown by thick, solid lines. Notations in the figure are (a and b : lattice unit vectors), (D : D -spacing along z), ($\lambda_r = \mathbf{b} $: ripple wavelength), (γ : oblique tilt angle), (A : ripple amplitude), (ψ : chain tilt angle with respect to the z direction), and (x_M : projected length of the major arm).	61
4.2	A picture of an annealing chamber. Need to take a picture	63
4.3	The horizontal profile of the beam used in the low resolution study. Each pixel was 0.07113 mm , which gave a CCD angular resolution $\Delta\theta$ of 0.0057° , corresponding to $\Delta q = 0.0011 \text{ \AA}^{-1}$ at the sample to detector distance of 359.7 mm . The beam FWHM = 1.7 pixels, giving $\Delta\theta = 0.010^\circ$ or $\Delta q = 0.0019 \text{ \AA}^{-1}$	66

4.4	The vertical profile of the beam used in the low resolution study. The beam height = 15 pixels = 1.1 mm.	66
4.5	1 second exposure (left) and 60 second exposure (right) of the low angle X-ray scattering from the DMPC ripple phase. The dark rectangle in the right image extending from $q_z = 0 \text{ \AA}^{-1}$ to 0.2 \AA^{-1} is the shadow cast by $100 \text{ }\mu\text{m}$ thick molybdenum beam stop. $D = 57.8 \text{ \AA}$, $\lambda_r = 145.0 \text{ \AA}$, and $\gamma = 97.8^\circ$. The gray scales used are [0 100] (left) and [0 500] (right).	68
4.6	CCD images of X-ray scattering taken with (left) and without (right) a nominally $25 \text{ }\mu\text{m}$ thick Mo attenuator. These data were taken at a fixed angle of incidence $\omega = 0.8^\circ$. The sample was an oriented film of DOPC:DOPE (3:1) in the fluid phase at 37°C . The wavelength was 1.175 \AA , the same as the one used for the ripple phase experiment. The same gray scale is used in both images. $100 \text{ pixel} = 0.11 \text{ \AA}^{-1}$ in q . A small dot located about $(p_x, p_z) = (520, 170)$ between the first and second orders is a specular reflection from the substrate. exposure time?	69
4.7	Vertical p_z slices of X-ray images shown in Fig. 4.6 (left). The scattering intensity measured with the attenuator (red solid circles) was multiplied by a factor of 6.9 and compared to the intensity measured without the attenuator (black solid circles, right). Exposure time? . .	70
4.8	The horizontal profile of the beam used in the high resolution experiment. The CCD angular resolution $\Delta\theta = 0.0092^\circ$ corresponding to $\Delta q = 0.0017 \text{ \AA}^{-1}$, at the sample to detector distance of 220.6 mm . The beam FWHM = $3.7 \text{ pixels} = 0.26 \text{ mm}$, giving $\Delta\theta = 0.034^\circ$ or $\Delta q = 0.0063 \text{ \AA}^{-1}$	72
4.9	The vertical profile of the beam used in the high resolution experiment. The beam height = 9 pixels = 0.64 mm	72
4.10	In-plane geometric broadening due to the sample width w_s and the beam width Δx_{beam} . A top view of the sample (green) on the Si wafer (gray) and the incoming and diffracted X-rays (bounded by red solid lines) are shown. The total in-plane scattering angle for a lipid chain-chain correlation is labeled as 2θ , and the geometric broadening as Δx	73

4.11	Schematics of the sample holder in the transmission mode. Side (left) and top (right) views are shown. The thickness of the Si wafer = 35 μm . The thickness of the sample $\approx 10 \mu\text{m}$. The distance between the axis of rotation and sample = 21.1 mm.	74
4.12	Picture of the sample holder looking from above. A lead tape was attached to the back of the sample holder to help reduce the background scattering, typically coming from the air gap between the flightpath snout and the mylar window of the chamber.	75
4.13	Circular path followed by the sample as the angle of incidence ω was changed. The sample to detector distance and D -spacing of the sample were measured in the LAXS mode, where $\omega = 1^\circ$. WAXS images were collected at the transmission mode, where $\omega = -45^\circ$. The z position of the sample was slightly higher at the LAXS mode than at the transmission mode, so the sample holder was vertically shifted for different modes.	75
4.14	Geometric broadening in TWAXS. The cross section of the incoming X-ray with the sample and the CCD detector are both shaded in red.	76
4.15	Top view of geometric broadening in TWAXS. The cross section of the incoming X-ray with the sample is shaded in red.	76
4.16	Side view of geometric broadening in TWAXS. The cross section of the outgoing X-ray with the CCD detector is shaded in red.	77
4.17	Projection of rectangular beam on the detector.	77
4.18	Experimental reflectivity geometry.	80
4.19	Ewald sphere construction for the ripple phase diffraction in the low angle regime. A ripple $k = 0$ peak is the solid, black circle on the q_z -axis. A ripple $k \neq 0$ ring is the black ring centered about the q_z -axis. The portion of the ring that is inside the Ewald sphere is shown as a red dashed line and the portion of the ring that is outside but behind the Ewald sphere is shown as a black dotted line. The magnitude of the total scattering angle is exaggerated. With a wavelength of 1.175 \AA , the magnitude $ \mathbf{k}_{\text{in}} = 5.35 \text{\AA}^{-1}$. For a $h = 5$ peak, $q_{50}^z = 0.54 \text{\AA}^{-1}$, one tenth of k_{in}	82
4.20	Side view of an arc of $k = 0$ peak shown as a thick blue line.	83

4.21	q -space representations of Bragg peaks and Bragg rings for $h = 1$ and 2 and $k = 0, 1$, and 2 in q_{hk}^z planes. The intersection between the Ewald sphere and a Bragg peak/ring is indicated in red. The observed intensity for the $k \neq 0$ orders is proportional to the fraction of the length of red arcs in the circumference. This fraction is equal to one for $k = 0$ reflections. Because the reflections are not in the same q_z plane, the range of q_y integration indicated by the height of the gray rectangle is different for different h orders. For $\gamma \neq 90^\circ$, the range of q_y integration is slightly different for different k reflections with the same h . The values shown are for $D = 58 \text{ \AA}$, $\lambda_r = 145 \text{ \AA}$, $\gamma = 90^\circ$, and $\lambda = 1.175 \text{ \AA}$. The magnitude of curvature of arcs is exaggerated.	84
4.22	The path of X-rays within the sample. The incident angle is ω and the total scattering angle is 2θ . An X-ray with a penetration depth of z is shown. The total thickness of the sample is t	87
4.23	Absorption factors as a function of $q_z \approx 4\pi\theta/\lambda$. The values at $q_z = 2\pi h/D$ corresponding to $D = 58 \text{ \AA}$ are shown as squares. $\mu = 2600 \text{ \mu m}^{-1}$, $t = 10 \text{ \mu m}$, and $\lambda = 1.175 \text{ \AA}$	89
4.24	NGIWAXS of the DMPC ripple phase for $D = 59.2 \text{ \AA}$ (left) and 60.8 \AA (right). The angle of incidence ω was 0.2° . The black regions around the edge of each image are the q -space that was not probed. The distorted, non rectangular shape of the probed q -space signifies non-linear relation between the CCD space and sample q -space.	95
4.25	Enlarged view of the right image in Fig. 4.24. To show smaller features around the peak, a different contrast is used.	96
4.26	q_r swaths, each averaged over 0.02 \AA^{-1} . The center q_z value of a swath is shown in the figure legends.	97
A.1	Two dimensional view of mosaic spread (left) and notations used in this section (right). The stacking direction of a perfect domain is \mathbf{n} and that of a tilted domain \mathbf{n}' . The deviation of \mathbf{n}' from \mathbf{n} denoted as α quantifies the degree of mis-orientation of a domain. The x , y , and z -axes are the sample coordinates.	101

A.2	Example of a two dimensional sample consisting of a perfect and tilted domains. $\mathbf{q} = (q_x, q_z)$ is the sample q -space and $\mathbf{q}' = (q'_x, q'_z)$ is the domain q -space. The two q -spaces are related by a rotation of α about the y -axis, which is into the page.	102
A.3	Notations used in this section. The arc originating from the Z -axis is the mosaic arc due to the mosaic spread distribution.	105
A.4	Rocking scan trace in q -space.	107

Chapter 4

Ripple Phase

When the temperature is reduced from the fluid phase, the ripple phase is observed in bilayers consisting of DMPC and DPPC lipids. This chapter discusses X-ray scattering experiments on the ripple phase formed by dimyristolphosphatidylcholine (DMPC) bilayers.

4.1 Introduction

(At some point, do some literature search and write up this section) The ripple phase has been a fascinating thermodynamic phase to many physicists and physical chemists since its discovery. It was originally observed in calorimetry study for alkanes by Sturtevant. Although this phase has never been reported to occur in a biologically relevant situation, it provides an interesting opportunity to study fundamental lipid interactions and their influence on the bilayer shape. (Let's find some recent papers and see if anyone says anything about biological relevance)

In the first structural study of this phase by Tardieu *et al.*, the X-ray diffraction pattern from DLPC was phased by a pattern recognition technique and the electron density map was calculated. It was shown that the structure corresponds to a 2D oblique unit cell shown in Fig. 4.1. The calculated electron density map showed that DLPC bilayers are height modulated and have a smooth, asymmetric shape. The ripple wavelength λ_r was reported to be 85.3 Å, the lamellar periodicity D 55.3 Å, and the oblique angle γ 110°. The electron density map reported the ripple amplitude $A = 15$ Å in DLPC.

Various experiments have indicated the existence of two types of ripple phases: the

stable asymmetric and the metastable symmetric phase. In the asymmetric phase, a plane of reflection perpendicular to the ripple wave vector is absent. The metastable symmetric phase has been seen in DPPC bilayers, but not in DMPC.

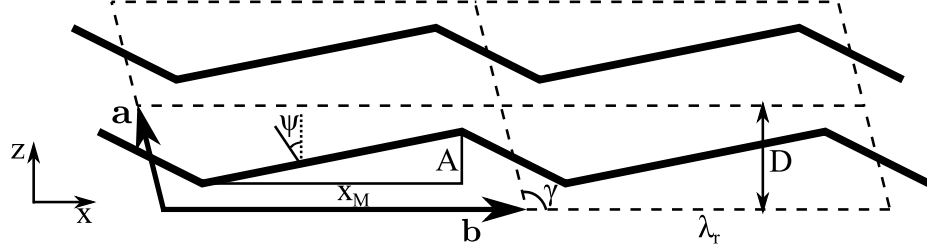


Figure 4.1: Lattice structure of the asymmetric ripple phase. Unit cells are shown in dash lines. Center of bilayers are shown by thick, solid lines. Notations in the figure are (**a** and **b**: lattice unit vectors), (D : D -spacing along z), ($\lambda_r = |\mathbf{b}|$: ripple wavelength), (γ : oblique tilt angle), (A : ripple amplitude), (ψ : chain tilt angle with respect to the z direction), and (x_M : projected length of the major arm).

The equilibrium structure of the ripple phase has been extensively studied by diffraction (X-ray [] and neutron []) and freeze fracture (AFM, electron microscopy [] and scanning tunneling microscopy []) techniques. In the scanning tunneling microscopy experiment [74], the three-dimensional contours of the ripple phase $P_{\beta'}$ of dimyristoylphosphatidylcholine (DMPC) were imaged, and a ripple wavelength of 130 Å and an amplitude of 45 Å were reported.

multilayer vs LUV. Any LUV paper report on ripple?

From X-ray data of the DMPC ripple of unoriented samples, Wack and Webb [1] argued that the ripples have a sawtooth shape, but were unable to phase the observed pattern. Their X-ray form factor data were later phased by employing a modeling and fitting technique by Sun *et al.* [75], and the electron density map was calculated, which indicated that the ripples indeed have a sawtooth shape. The map also showed that the major arm is about twice as long as the minor arm. The bilayer thickness was found to be larger than that of the minor arm. The value of the bilayer thickness in the major arm was comparable to the thickness of DMPC bilayers in the gel phase whereas the thickness of the minor arm was comparable to that in the fluid phase.

A structural investigation by X-ray diffraction of the ripple phase of oriented dipalmitoylphosphatidylcholine (DPPC) samples indicated that hydrocarbon chains are packed in a hexagonal lattice with chains tilted in the plane perpendicular to the ripple wave vector [76]. In that study, the oblique angle γ was found to be 90°.

Katsaras and Raghathan papers

Several MD (molecular dynamics) simulations have been carried out, indicating various lipid packing. de Vrie *et al.* has suggested interdigitated chain in the minor side [77].

Some theory papers

D (Å)	λ_r (Å)	γ (deg)
55.0	159.4	99.0
57.0	140.8	97.6
57.3	151.6	97.8
57.4	148.4	97.6
57.5	144.1	97.8
57.5	141.9	98.0
58.0	140.1	98.2
57.8	145.0	98.2
58.0	141.7	98.4
59.8	129.6	97.3
60.6	130.1	97.0
61.5	130.8	96.5
62.4	122.0	95.9
63.9	123.1	94.9
64.9	120.3	92.3

Table 4.1: Lattice constants for DMPC at $T = 18.0^\circ\text{C}$ reported by Wack and Webb [1]. The data collected and analyzed in this thesis are colored blue.

4.2 Materials and Methods

4.2.1 Sample Preparation

DMPC was purchased from Avanti Polar Lipids and used without further purification. Oriented thin films were deposited on clean silicon wafers with a chloroform:methanol 2:1 (volume ratio) mixture following the rock and roll procedure [78]. In previous synchrotron experiments, the samples were created and annealed more than a week in advance and stored in a refrigerator. The quality of these samples measured by their mosaic spread was found to worsen over time after the samples were annealed. Therefore, to ensure the best sample quality, the samples were annealed for approximately

12 hours just before the X-ray experiment. Figure 4.2 shows a picture of the annealing chamber. To achieve gentle but efficient hydration of a sample, filter papers were installed. For successful annealing, it must be emphasized that the annealing chamber should equilibrate in an annealing oven prior to putting a sample in the chamber. When a sample was put in the chamber sitting at a room temperature and then the system was placed inside the oven, warmer water vapor inside the chamber condensed on the cooler sample, causing so called flooding of oriented sample. A small drop of water on an oriented film is detrimental for the orientation quality because the entropy-driven formation of unilamellar vesicles causes oriented bilayers to peel off one by one.

Figure 4.2: A picture of an annealing chamber. Need to take a picture

The sample for the grazing incident wide angle study was prepared in the same way as for low angle study. In order to minimize the geometric broadening, the sample was trimmed to 1 mm in width along the beam direction.

The sample for transmission study was deposited on a thin, 35 micron, silicon wafer, and oriented following the rock and roll procedure [78]. See also Sec. 3.2.1. Because the wafer was very fragile, attaching the sample to a sticky thing was impossible. Instead, the sample was attached to a plastic cap on a small vial with a small amount of heat sink compound at a corner of the wafer. The wafer was stable enough for rocking.

4.2.2 Instrumental Resolution

Talk about divergence, dispersion, and geometric broadening.

Divergence

Energy dispersion

multilayer vs Si crystal

Geometric Broadening

WAXS vs LAXS Make a table (in pixel and q)

4.2.3 Low Angle X-ray Scattering Experiment

(Transmission was in 2011) The low resolution X-ray scattering experiment was carried out at the Cornell High Energy Synchrotron Source (CHESS) G1 station in three different runs (2011, 2012, and 2013). The low angle X-ray scattering (LAXS) data analyzed in this thesis were collected in 2013. The X-ray beam was set up by the station scientist, Dr. Arthur Woll. A W/B₄C multilayer monochromator with energy bandwidth $\Delta E/E$ of 1.5% was used, providing a very intense X-ray beam. The energy of the X-ray beam was 10.55 keV, corresponding to a wavelength of 1.175 Å. The horizontal and vertical divergence of the beam were 4.2×10^{-5} rad and 1.6×10^{-4} rad, respectively. The beam shape, measured through a semi-transparent 200 μm thick molybdenum (Mo) beam stop, is shown in Fig. 4.3 and 4.4. The horizontal beam width was 2.3 pixels (0.16 mm). The vertical beam width was approximately 1 mm, tall enough to cover the entire sample when the sample was tilted by 7°. The sample was rocked during X-ray exposure between -1.6° and 7° in order to observe many diffraction peaks in one data collection. The sample to detector distance was 359.7 mm, measured by indexing silver behenate Bragg peaks. The D-spacing of silver behenate is known to be 58.367 Å.

Occasionally, sheets of molybdenum (Mo), each nominally 25 μm were used to attenuate the incoming beam. These sheets were installed by Dr. Arthur Woll in the upstream of the sample chamber. The attenuation length μ of 10.55 keV X-ray in Mo is 13.74 μm [79]. For a 25 μm thick Mo attenuator, the attenuation factor is calculated to be $[\exp(-25/13.74)]^{-1} = 6.2$. The exact attenuation factor was determined by comparing X-ray images collected with and without the attenuator, shown in Fig. 4.6 and 4.7. The attenuation factor of the nominally 25 μm thick Mo was found to be 6.9 for the wavelength used (1.175 Å).

Sheets of Mo were also used as a beam stop downstream of the sample, just outside the hydration chamber, to attenuate the beam and strong orders. 100 and 200 μm were used to attenuate strong orders and 225 μm to attenuate the beam. To avoid saturation of CCD pixels by the very intense beam, the beam stop was always set to block the beam.

A few Bragg peaks in the low angle X-ray scattering of the ripple phase were very strong, leading to saturation of CCD pixels for data collection with a long exposure time. In order to probe a wide range of q -space, three images were taken: 1) a short, one second exposure with a nominally 25 micron molybdenum attenuator installed in

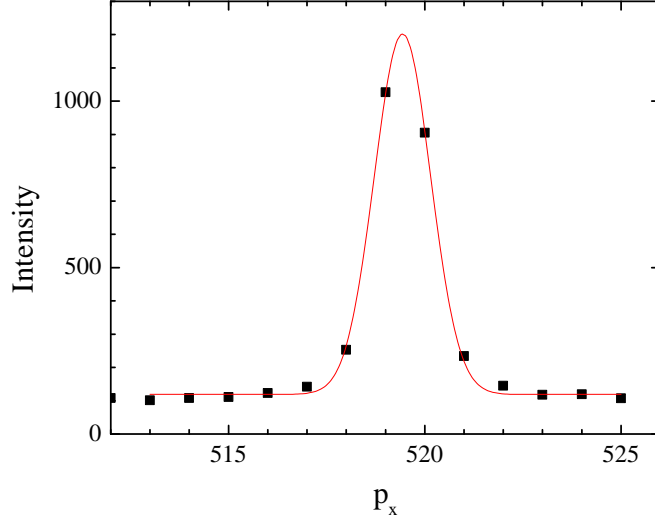


Figure 4.3: The horizontal profile of the beam used in the low resolution study. Each pixel was 0.07113 mm, which gave a CCD angular resolution $\Delta\theta$ of 0.0057° , corresponding to $\Delta q = 0.0011 \text{ \AA}^{-1}$ at the sample to detector distance of 359.7 mm. The beam FWHM = 1.7 pixels, giving $\Delta\theta = 0.010^\circ$ or $\Delta q = 0.0019 \text{ \AA}^{-1}$.

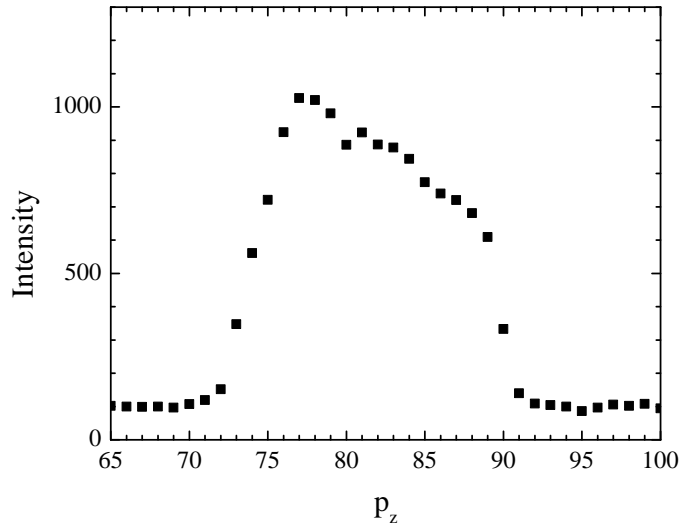


Figure 4.4: The vertical profile of the beam used in the low resolution study. The beam height = 15 pixels = 1.1 mm.

the upstream of the sample to reduce the intensity of the incoming X-ray beam, 2) one second exposure without the beam attenuator, and 3) 60 second exposure with a beam stop blocking the very intense (1,0) and (2,0) peaks. See Fig. 4.5. Then, the integrated intensity of (1,0) peak was measured from the first image. This value was multiplied by 6.9 to account for the beam attenuation and by 60 to scale with the exposure time. The intensity of (2,0) and (2,-1) were measured from the second image, also multiplied by 60 to account for the shorter exposure time. The intensity of the rest of the observed peaks were measured from the third image.

The integrated intensity of each peak was obtained using the Nagle lab tvview software developed by Dr. Yufeng Liu [39] by putting a box around a peak and summing up the intensity in those pixels that fall inside the box. The background scattering was estimated by measuring the intensity in pixels near the peak but not containing any peak tail. The choice of box size was made according to the width of each peak. Because of mosaic spread in the sample, the peaks were wider for higher orders. Consequently, the box was made wider for higher orders. The box size was chosen so that approximately 80% of the peak intensity was counted toward the integrated intensity.

4.2.4 Near Grazing Incidence Wide Angle X-ray Scattering Experiment

The high resolution X-ray scattering experiment was also carried out at the G1 station. To achieve a higher instrumental resolution than that for the low angle X-ray scattering experiment described in a previous section, a (111) silicon monochromator was used, which gave $\Delta E/E$ of 0.01%. Due to the geometry of the G1 station, the Si monochromator was placed in the G1 hutch, in series with the multilayer monochromator. The instrument was set up by the G1 station scientist, Author Woll, and the assistant scientist, Dr. Robin Baur.

The energy of the beam was 10.55 keV (wavelength = 1.175 Å). The horizontal and vertical divergence of the X-ray beam were 4.2×10^{-5} rad and 1.6×10^{-4} rad, respectively. The horizontal beam width was 4 pixels (0.28 mm) as shown in Fig. ???. With this beam, the scattering resolution in the wide angle region was dominated by the geometric broadening. The broadening was due to the sample width along the beam direction and the horizontal beam width (Fig. 4.10. From the geometry of the

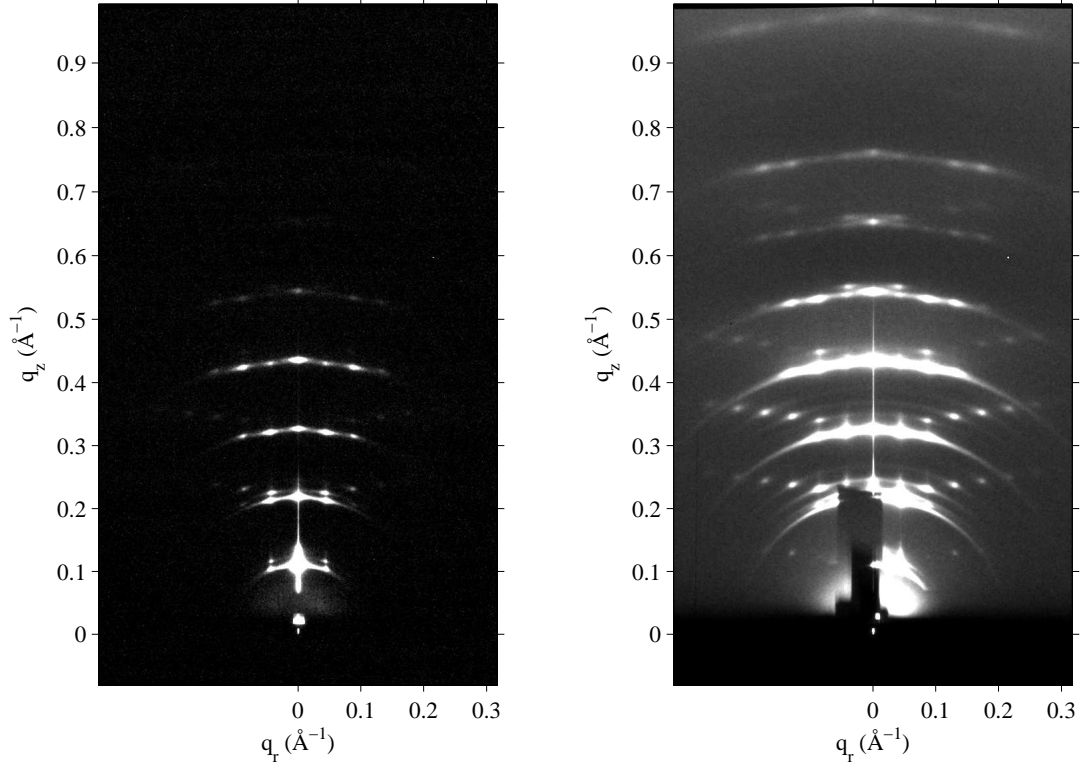


Figure 4.5: 1 second exposure (left) and 60 second exposure (right) of the low angle X-ray scattering from the DMPC ripple phase. The dark rectangle in the right image extending from $q_z = 0 \text{ \AA}^{-1}$ to 0.2 \AA^{-1} is the shadow cast by $100 \text{ }\mu\text{m}$ thick molybdenum beam stop. $D = 57.8 \text{ \AA}$, $\lambda_r = 145.0 \text{ \AA}$, and $\gamma = 97.8^\circ$. The gray scales used are $[0 \text{ } 100]$ (left) and $[0 \text{ } 500]$ (right).

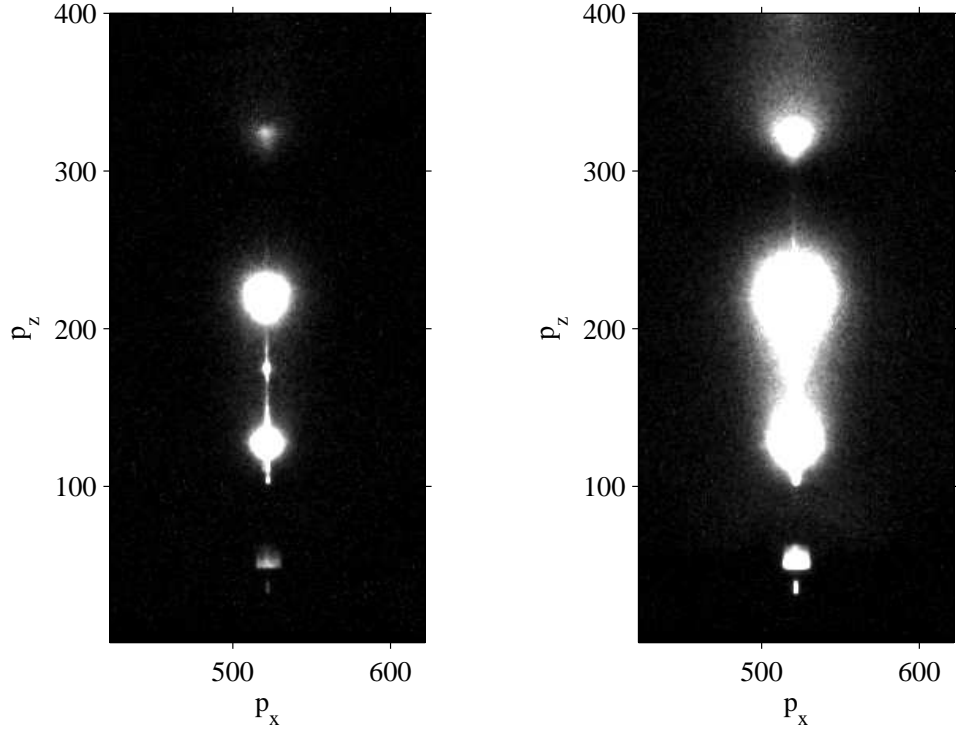


Figure 4.6: CCD images of X-ray scattering taken with (left) and without (right) a nominally $25\ \mu\text{m}$ thick Mo attenuator. These data were taken at a fixed angle of incidence $\omega = 0.8^\circ$. The sample was an oriented film of DOPC:DOPE (3:1) in the fluid phase at $37\ ^\circ\text{C}$. The wavelength was $1.175\ \text{\AA}$, the same as the one used for the ripple phase experiment. The same gray scale is used in both images. $100\ \text{pixel} = 0.11\ \text{\AA}^{-1}$ in q . A small dot located about $(p_x, p_z) = (520, 170)$ between the first and second orders is a specular reflection from the substrate. **exposure time?**

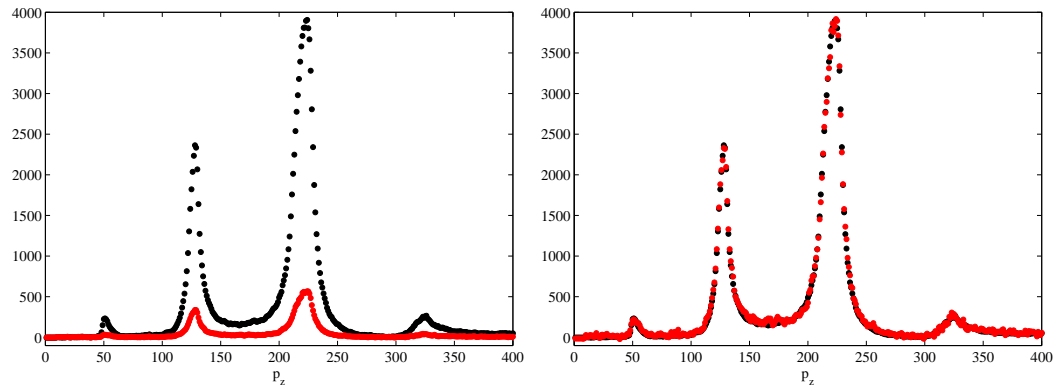


Figure 4.7: Vertical p_z slices of X-ray images shown in Fig. 4.6 (left). The scattering intensity measured with the attenuator (red solid circles) was multiplied by a factor of 6.9 and compared to the intensity measured without the attenuator (black solid circles, right). Exposure time?

experiment, the geometric broadening Δx can be determined,

$$\Delta x = \Delta x_{\text{beam}} + w_s \tan(2\theta).$$

The total scattering angle 2θ for the ripple WAXS was approximately 16° . To minimize the contribution from the sample, the sample was trimmed to 1 mm along the beam direction. (edge effect)The width of 1 mm was chosen because (1) I could not trim more without a more sophisticated device than a simple razor blade, (2) a very narrow sample would be a weak scattering body, and (3) any effect from the sample edge might become too significant to ignore. Given the above reasons and due to limited availability of synchrotron beam time, I considered a 1 mm width to be reasonable. With these values, the resolution is $\Delta x = 0.57 \text{ mm} = 8 \text{ pixels}$, which would be the unresolved width of an intrinsically infinitely sharp wide angle peak. The sample to detector distance were 220.6 mm, measured using silver behenate. Then, the minimum peak width measured in q -space would be $\Delta q \approx 0.014 \text{ \AA}^{-1}$. Wide angle X-ray scattering was collected at an incident angle of 0.2° . The total external reflection from an air-lipid interface occurs approximately at 0.1° and 0.17° for air-silicon interface, so 0.2° is not quite grazing incidence. Grazing incidence usually implies that the incident angle is less than the critical angle for a total external reflection. Therefore, 0.2° is called near grazing incidence in this thesis.

4.2.5 Transmission Wide Angle X-ray Scattering Experiment

The transmission wide angle X-ray scattering (TWAXS) experiment was also carried out at the G1 station, and a similar instrumental resolution to the one in Sec. 4.2.3 was used. The sample to detector distance was measured to be 170 mm using silver behenate when the angle of incidence ω was 0° . The incident angle was set to -45° for transmission data collection. A $35 \text{ }\mu\text{m}$ thick silicon substrate absorbs an X-ray at 10.5 keV by 20% [79]. To measure a D-spacing, mosaic spread of the sample was exploited. Unfortunately, the axis of the rotation motor did not coincide with the sample axis, so the sample to detector distance varied as ω was varied. To accurately measure the sample to detector distance, low angle scattering was collected at a fixed ω . Due to the sample mosaic spread, many orders were visible. While the relative intensity of each order was inaccurate, the position of peaks was the same as that observed with a rotating sample. The sample to detector distance was accurately measured at $\omega =$

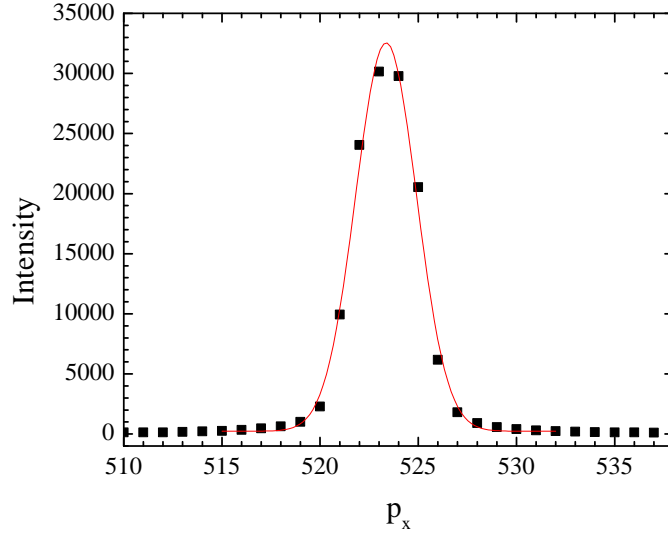


Figure 4.8: The horizontal profile of the beam used in the high resolution experiment. The CCD angular resolution $\Delta\theta = 0.0092^\circ$ corresponding to $\Delta q = 0.0017 \text{ \AA}^{-1}$, at the sample to detector distance of 220.6 mm. The beam FWHM = 3.7 pixels = 0.26 mm, giving $\Delta\theta = 0.034^\circ$ or $\Delta q = 0.0063 \text{ \AA}^{-1}$.

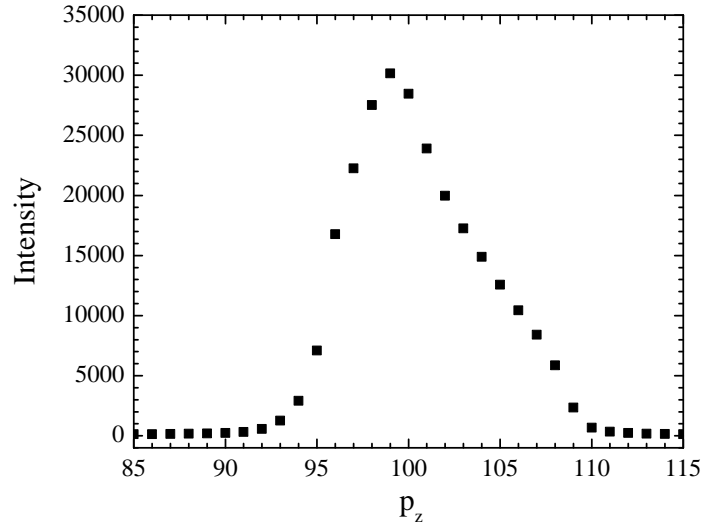


Figure 4.9: The vertical profile of the beam used in the high resolution experiment. The beam height = 9 pixels = 0.64 mm.

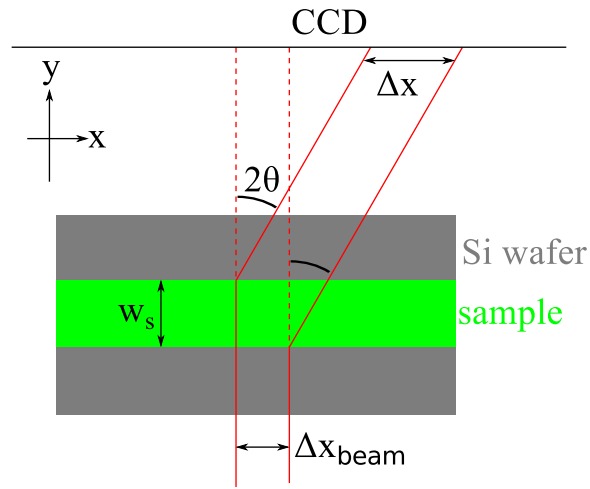


Figure 4.10: In-plane geometric broadening due to the sample width w_s and the beam width Δx_{beam} . A top view of the sample (green) on the Si wafer (gray) and the incoming and diffracted X-rays (bounded by red solid lines) are shown. The total in-plane scattering angle for a lipid chain-chain correlation is labeled as 2θ , and the geometric broadening as Δx .

0° using a silver behenate sample. From the geometry of the sample holder, a shift in the sample to detector distance was estimated for an arbitrary incident angle ω .

Explain how we estimated the sample to detector distance at $\omega = -45^\circ$. Explain how we leveled the sample (using the sample scattering and ascan). The background scattering was collected by replacing the sample with a bare wafer.

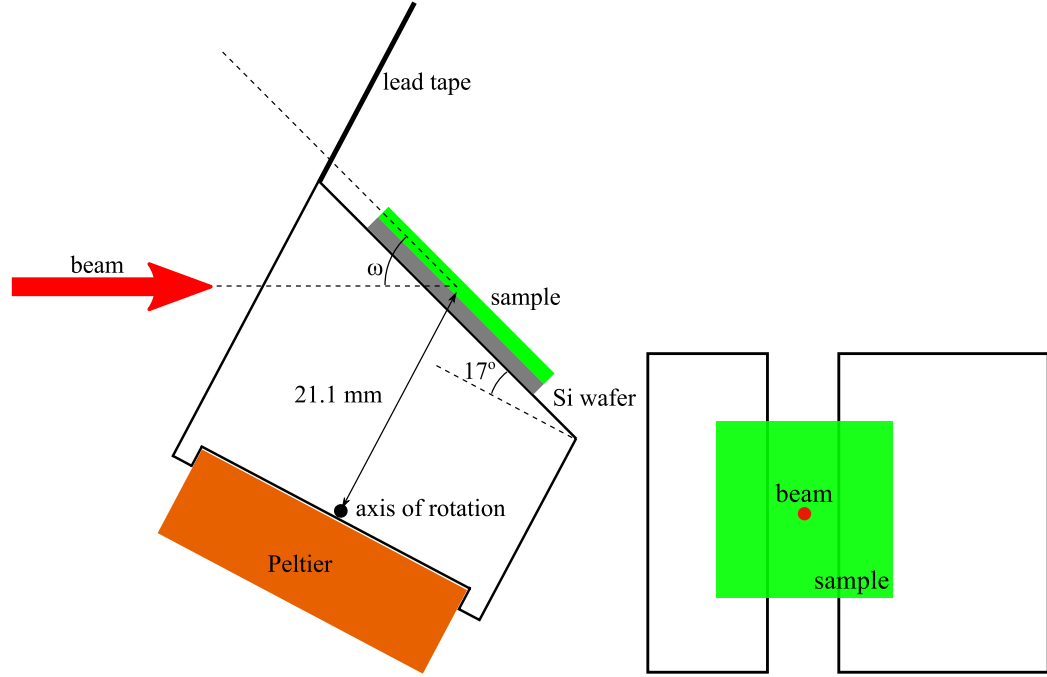


Figure 4.11: Schematics of the sample holder in the transmission mode. Side (left) and top (right) views are shown. The thickness of the Si wafer = $35 \mu\text{m}$. The thickness of the sample $\approx 10 \mu\text{m}$. The distance between the axis of rotation and sample = 21.1 mm.

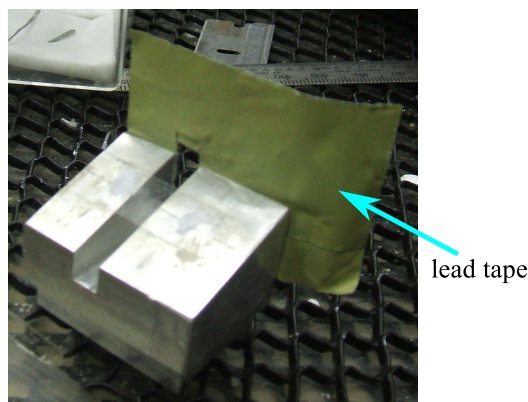


Figure 4.12: Picture of the sample holder looking from above. A lead tape was attached to the back of the sample holder to help reduce the background scattering, typically coming from the air gap between the flightpath snout and the mylar window of the chamber.

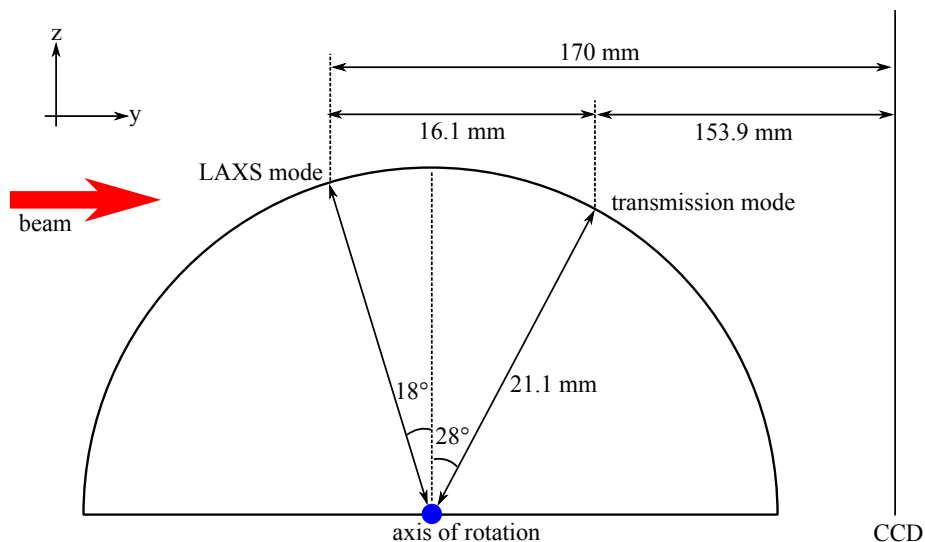


Figure 4.13: Circular path followed by the sample as the angle of incidence ω was changed. The sample to detector distance and D -spacing of the sample were measured in the LAXS mode, where $\omega = 1^\circ$. WAXS images were collected at the transmission mode, where $\omega = -45^\circ$. The z position of the sample was slightly higher at the LAXS mode than at the transmission mode, so the sample holder was vertically shifted for different modes.

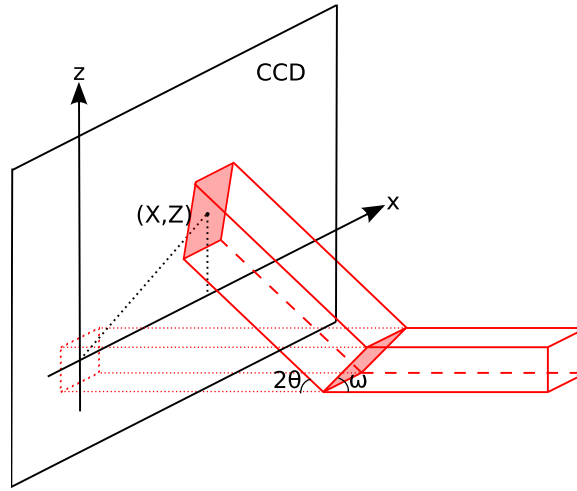


Figure 4.14: Geometric broadening in TWAXS. The cross section of the incoming X-ray with the sample and the CCD detector are both shaded in red.

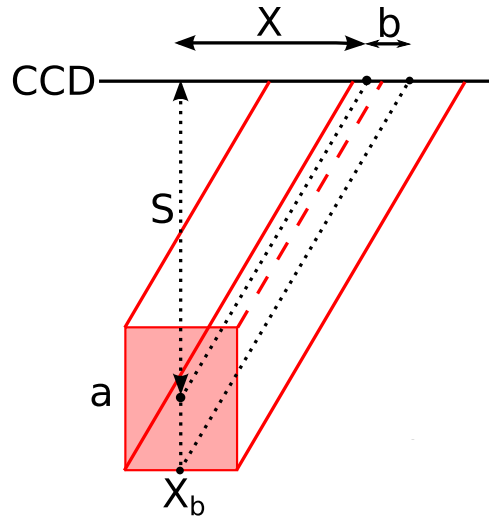


Figure 4.15: Top view of geometric broadening in TWAXS. The cross section of the incoming X-ray with the sample is shaded in red.

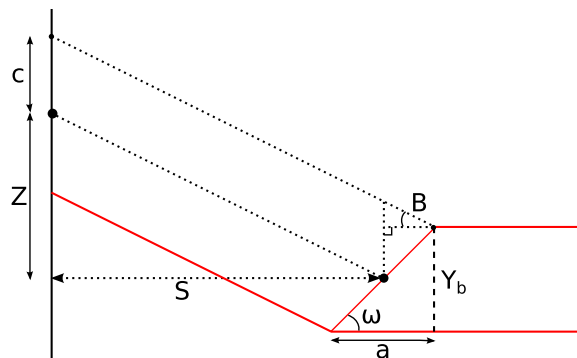


Figure 4.16: Side view of geometric broadening in TWAXS. The cross section of the outgoing X-ray with the CCD detector is shaded in red.

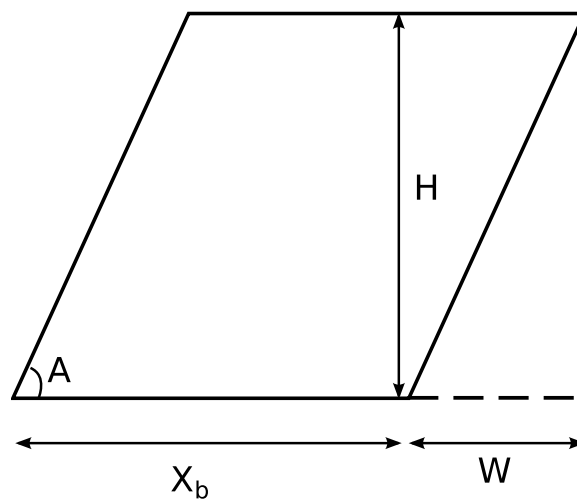


Figure 4.17: Projection of rectangular beam on the detector.

4.3 LAXS analysis

4.3.1 Lattice Structure

The unit cell vectors for the two-dimensional oblique lattice shown in Fig. 4.1 can be expressed as

$$\mathbf{a} = \frac{D}{\tan \gamma} \hat{\mathbf{x}} + D \hat{\mathbf{z}} \quad (4.1)$$

and

$$\mathbf{b} = \lambda_r \hat{\mathbf{x}}. \quad (4.2)$$

The corresponding reciprocal lattice unit cell vectors are

$$\mathbf{A} = \frac{2\pi}{D} \hat{\mathbf{z}} \quad (4.3)$$

and

$$\mathbf{B} = \frac{2\pi}{\lambda_r} \hat{\mathbf{x}} - \frac{2\pi}{\lambda_r \tan \gamma} \hat{\mathbf{z}}. \quad (4.4)$$

The reciprocal lattice vector, \mathbf{q}_{hk} for the Bragg peak with Miller indices (h, k) is

$$\mathbf{q}_{hk} = h\mathbf{A} + k\mathbf{B}, \quad (4.5)$$

so its Cartesian components are

$$\mathbf{q}_{hk} \cdot \hat{\mathbf{x}} = q_{hk}^x = \frac{2\pi k}{\lambda_r} \equiv q_k^x \quad (4.6)$$

$$\mathbf{q}_{hk} \cdot \hat{\mathbf{y}} = q_{hk}^y = 0 \quad (4.7)$$

$$\mathbf{q}_{hk} \cdot \hat{\mathbf{z}} = q_{hk}^z = \frac{2\pi h}{D} - \frac{2\pi k}{\lambda_r \tan \gamma}. \quad (4.8)$$

Our sample consists of many ripple domains with a uniform distribution of in-plane directions of the ripple wave vector, \mathbf{b} in Fig. 4.1. In this case, q_{hk}^x and q_{hk}^y are combined to give $q_{hk}^r = 2\pi k/\lambda_r$.

4.3.2 Sample q -space

The incoming and outgoing wavevectors of the x-ray beam in Fig. 4.18 are given by

$$\mathbf{k}_{\text{in}} = \frac{2\pi}{\lambda} \hat{\mathbf{y}}, \quad \mathbf{k}_{\text{out}} = \frac{2\pi}{\lambda} (\sin 2\theta \cos \phi \hat{\mathbf{x}} + \cos 2\theta \hat{\mathbf{y}} + \sin 2\theta \sin \phi \hat{\mathbf{z}}), \quad (4.9)$$

where λ is the wavelength of x-ray, 2θ is the total scattering angle, and ϕ is the angle measured from the equator on the detector. The scattering vector (also called momentum transfer vector) is the difference between \mathbf{k}_{in} and \mathbf{k}_{out} ,

$$\begin{aligned} \mathbf{q} &= \mathbf{k}_{\text{out}} - \mathbf{k}_{\text{in}} \\ &= q (\cos \theta \cos \phi \hat{\mathbf{x}} - \sin \theta \hat{\mathbf{y}} + \cos \theta \sin \phi \hat{\mathbf{z}}), \end{aligned} \quad (4.10)$$

where $q = 4\pi \sin \theta / \lambda$ is the magnitude of the scattering vector. When the sample is rotated by ω about the lab x-axis in the clockwise direction as shown in Fig. 4.18, the sample q -space also rotates and are given by

$$\hat{\mathbf{e}}_{\mathbf{x}} = \hat{\mathbf{x}}, \quad \hat{\mathbf{e}}_{\mathbf{y}} = \cos \omega \hat{\mathbf{y}} + \sin \omega \hat{\mathbf{z}}, \quad \hat{\mathbf{e}}_{\mathbf{z}} = -\sin \omega \hat{\mathbf{y}} + \cos \omega \hat{\mathbf{z}}. \quad (4.11)$$

From Eq. (4.10) and (4.11), we find Cartesian components of the sample q -space to be

$$\begin{aligned} q_x &= \mathbf{q} \cdot \hat{\mathbf{e}}_{\mathbf{x}} = q \cos \theta \cos \phi, \\ q_y &= \mathbf{q} \cdot \hat{\mathbf{e}}_{\mathbf{y}} = q (-\sin \theta \cos \omega + \cos \theta \sin \phi \sin \omega), \\ q_z &= \mathbf{q} \cdot \hat{\mathbf{e}}_{\mathbf{z}} = q (\sin \theta \sin \omega + \cos \theta \sin \phi \cos \omega). \end{aligned} \quad (4.12)$$

The position, (X, Z) , of a CCD pixel is measured with respect to the beam and given by

$$X = S \tan 2\theta \cos \phi, \quad Z = S \tan 2\theta \sin \phi, \quad (4.13)$$

where S is the distance between the sample and detector.

From a model for the electron density of a lipid bilayer, one calculates the X-ray scattering intensity pattern, $I(\mathbf{q})$. Then, Eq. (4.12) and (4.13) relate $I(\mathbf{q})$ to the experimentally measured intensity pattern, $I(X, Z)$. It is important to remember that a given pixel position, (X, Z) , corresponds to a triplet (q_x, q_y, q_z) . Fully exploring the sample q -space requires changing ω for a fixed wavelength, which was achieved

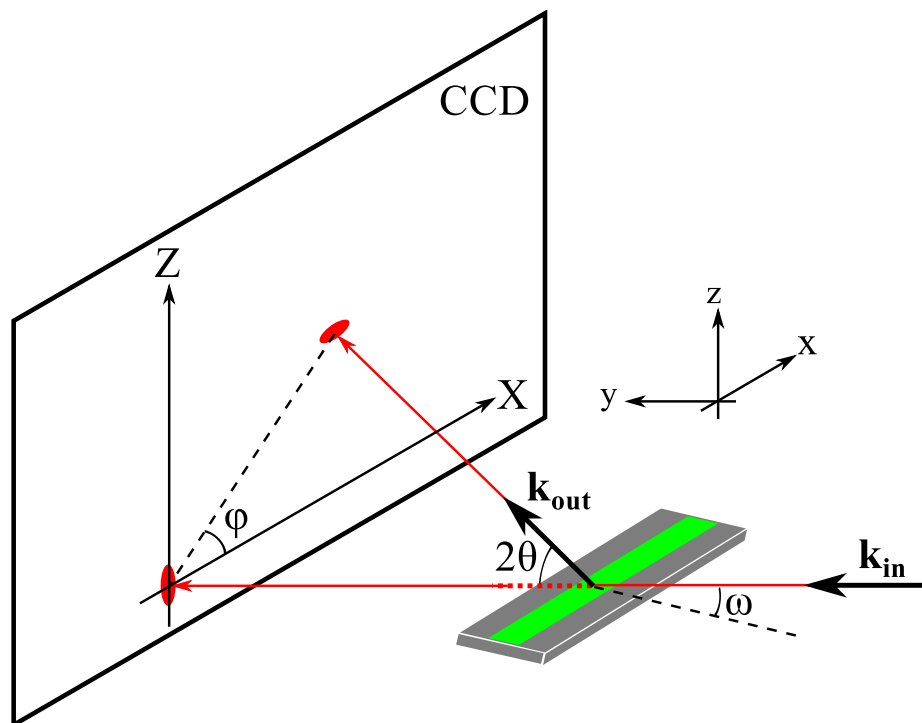


Figure 4.18: Experimental reflectivity geometry.

by continuously rotating the sample with a motor. In the ripple phase, because our sample has in-plane rotational symmetry, the ripple side peaks ($h, k \neq 0$) make up Bragg rings while the main peaks ($h, k = 0$) are still delta function like (see Fig. 4.19) in q -space. In order for the main peak to be observed, ω must be equal to θ_B , but the side peaks are observed at any ω . Those side peaks get slightly smeared due to integration over q_y .

For low angle x-ray scattering (LAXS), it is convenient to linearize the above equations in terms of θ and ω . In the small angle approximation, $\sin \phi \approx Z/(2S\theta)$ and $\cos \phi \approx X/(2S\theta)$, and

$$\begin{aligned} q_x &\approx \frac{4\pi\theta \cos \phi}{\lambda} \approx kX/S \\ q_y &\approx q_z\omega - \frac{4\pi\theta^2}{\lambda} \approx q_z\omega - \frac{\lambda q_z^2}{4\pi} \\ q_z &\approx \frac{4\pi\theta \sin \phi}{\lambda} \approx kZ/S, \end{aligned} \tag{4.14}$$

with $k = 2\pi/\lambda$. For wide angle X-ray scattering, the exact relations given by Eq. (4.12) are necessary. Especially in the transmission experiment, where ω is large, an observed X-ray pattern appears nontrivial and becomes almost impossible to analyze without the use of Eq. (4.12). The transmission experiment is discussed in Sec.4.5.3.

4.3.3 Lorentz Correction

Our sample has in-plane rotational symmetry about the z -axis. Ignoring mosaic spread to which we will come back later, this means that the sample consists of many domains with differing ripple directions, all domains being parallel to the substrate. In sample q -space, ripple ($h, k \neq 0$) side peaks are represented as rings centered at the meridian, or q_z -axis, while ($h, k = 0$) main peaks are still points on the meridian (see Fig. 4.19). Then, for an arbitrary incident angle ω , ($h, 0$) peaks are not observed while side peaks are observed for a range of ω as will now be explained.

In order to capture all (h, k) peaks in one X-ray exposure, the sample was continuously rotated over a range of ω , $\Delta\omega$, about the x -axis. As a result of this rotation, the ($h, 0$) main peaks become arcs that subtend an angle $\Delta\omega$, as shown in Fig. 4.20, with its length equal to $\Delta\omega q_{h0}^z$. The detector records the intersections of these arcs

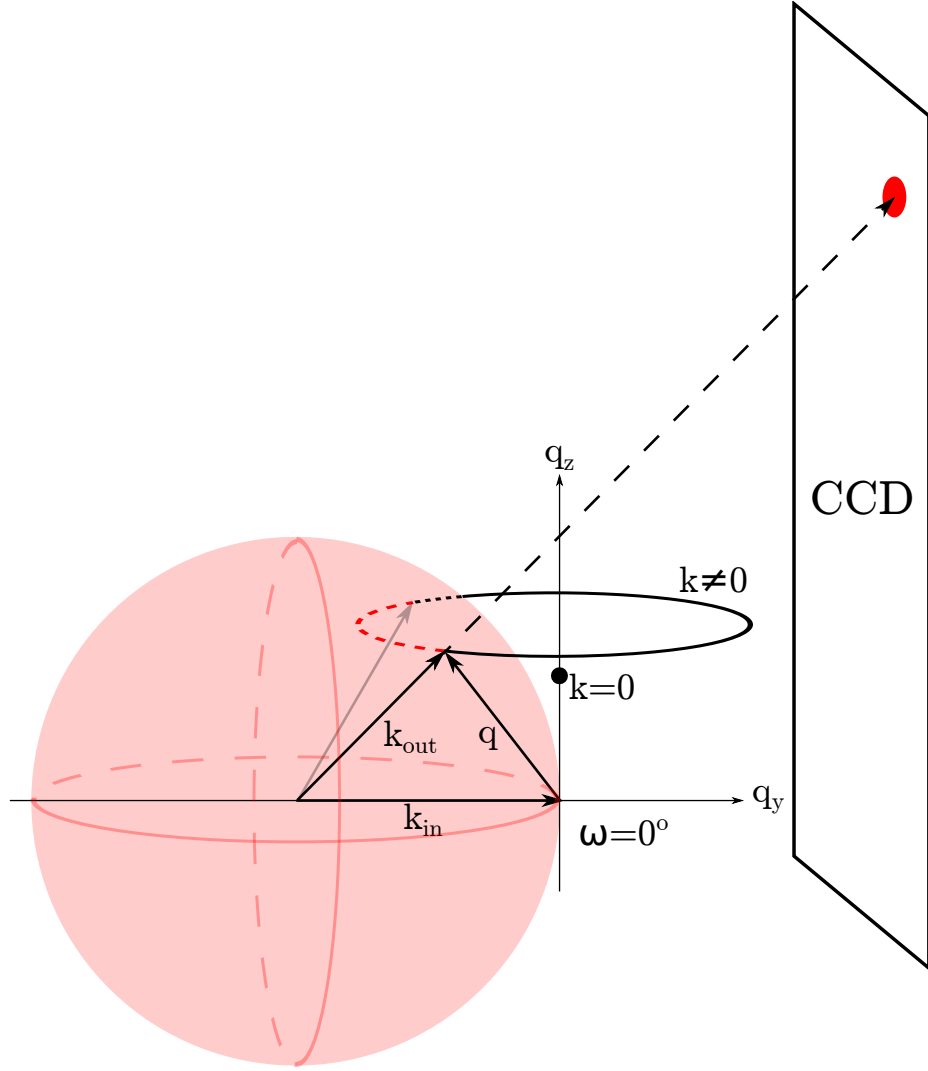


Figure 4.19: Ewald sphere construction for the ripple phase diffraction in the low angle regime. A ripple $k = 0$ peak is the solid, black circle on the q_z -axis. A ripple $k \neq 0$ ring is the black ring centered about the q_z -axis. The portion of the ring that is inside the Ewald sphere is shown as a red dashed line and the portion of the ring that is outside but behind the Ewald sphere is shown as a black dotted line. The magnitude of the total scattering angle is exaggerated. With a wavelength of 1.175 \AA , the magnitude $|\mathbf{k}_{in}| = 5.35 \text{ \AA}^{-1}$. For a $h = 5$ peak, $q_{50}^z = 0.54 \text{ \AA}^{-1}$, one tenth of k_{in} .

with the Ewald sphere, so the intrinsic scattering intensity of the $(h, k = 0)$ reflections is the product of the observed intensity, I_{hk}^{obs} with the arc length, that is,

$$I_{h0} = \Delta\omega q_{h0}^z I_{h0}^{\text{obs}}. \quad (4.15)$$

This is the usual Lorentz correction for lamellar orders.

Now, we consider relative intensity of side peaks for a given order h . As described earlier, $(h, k \neq 0)$ side peaks are represented as rings whose radius is q_{hk}^r in the sample q -space. Because only the domains with the right ripple direction can satisfy the Bragg's condition at a given fixed angle ω , the intrinsic scattering intensity in this ring is reduced by a factor of $2\pi q_k^r$ compared to the $(h, 0)$ reflections. This reduction of intensity can be nicely visualized by the Ewald sphere construction shown in Fig. 4.19, which shows that the entire rings are not intersected by the Ewald sphere at a fixed angle. Then, the intrinsic scattering intensity in a ring is

$$I_{hk \neq 0} \propto 2\pi q_{hk}^r I_{hk}^{\text{obs}}. \quad (4.16)$$

During an X-ray exposure, the sample q -space rotates and the rings are intersected by the Ewald sphere at all our experimental incident angles ω . However, as Fig. 4.21 shows, only small parts of the rings are actually intersected with the Ewald sphere. To obtain the full expression for $(h, k \neq 0)$ reflections, we now turn to a more rigorous calculation.

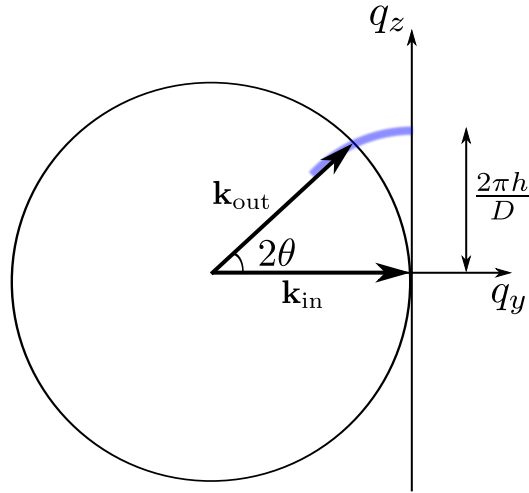


Figure 4.20: Side view of an arc of $k = 0$ peak shown as a thick blue line.

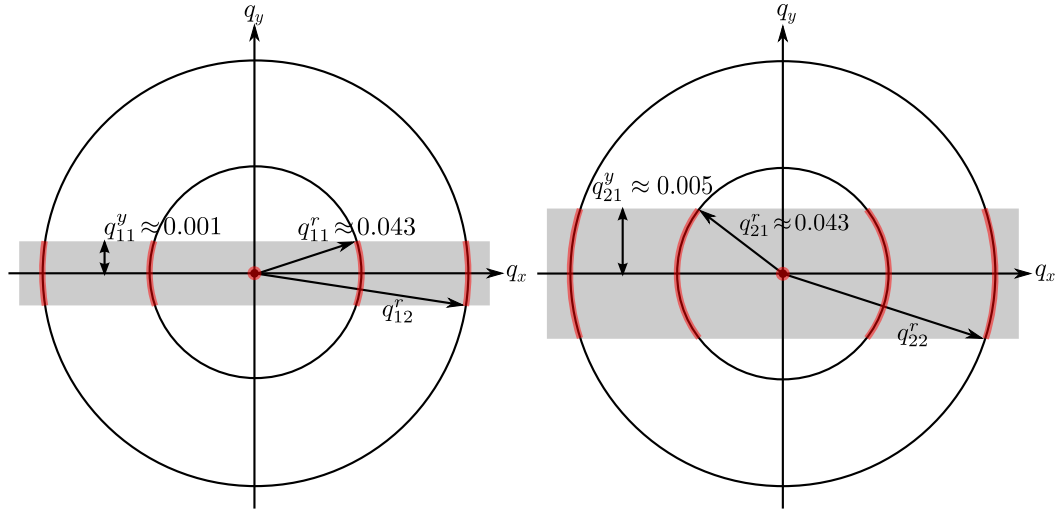


Figure 4.21: q -space representations of Bragg peaks and Bragg rings for $h = 1$ and 2 and $k = 0, 1$, and 2 in q_{hk}^z planes. The intersection between the Ewald sphere and a Bragg peak/ring is indicated in red. The observed intensity for the $k \neq 0$ orders is proportional to the fraction of the length of red arcs in the circumference. This fraction is equal to one for $k = 0$ reflections. Because the reflections are not in the same q_z plane, the range of q_y integration indicated by the height of the gray rectangle is different for different h orders. For $\gamma \neq 90^\circ$, the range of q_y integration is slightly different for different k reflections with the same h . The values shown are for $D = 58$ Å, $\lambda_r = 145$ Å, $\gamma = 90^\circ$, and $\lambda = 1.175$ Å. The magnitude of curvature of arcs is exaggerated.

Mathematically, the rotation is equivalent to an integration over ω . In low angle X-ray scattering, q_z is nearly constant at a given pixel as ω is changed, which can be seen from Eq. (4.14). As Eq. (4.14) shows, ω dependence appears only through q_y , so rotating the sample is realized by integrating over q_y ; formally, we write $d\omega = dq_y/q_z$. To derive the integration limits on q_y , let us consider two cases: (1) When $\omega \leq 0$, the incoming X-ray beam is blocked by the back of the substrate. This sets the lower limit of ω to 0. Plugging $\omega = 0$ in Eq. 4.14), we find the lower limit of the q_y integration to be $-\lambda q_z^2/(4\pi)$. (2) When $\omega \geq 2\theta$, the substrate blocks the outgoing X-ray, so the maximum $\omega = 2\theta$. Within the small angle approximation, $q_z \approx 4\pi\theta/\lambda$. Then, the maximum ω can be expressed as $\lambda q_z/(2\pi)$. Plugging this expression for ω in Eq. (4.14), we find the upper limit of the q_y integration to be $\lambda q_z^2/(4\pi)$. Also integrating over the detector pixels X and Z to obtain integrated intensity, we write the observed intensity as

$$\begin{aligned} I_{hk}^{\text{obs}} &\propto \int dX \int dZ \int d\omega I_{hk} \\ &\propto \int dq_x \int dq_z \int_{-\frac{\lambda q_z^2}{4\pi}}^{\frac{\lambda q_z^2}{4\pi}} \frac{dq_y}{q_z} I_{hk}(\mathbf{q}), \end{aligned} \quad (4.17)$$

where $1/q_z$ factor in q_y integration is the usual Lorentz polarization factor in the small angle approximation.

For a crystalline sample with in-plane rotational symmetry, the structure factor of a ripple Bragg peak is

$$S_{hk}(\mathbf{q}) = S_{hk}(q_r, q_z) = \frac{1}{2\pi q_r} \delta(q_r - q_{hk}^r) \delta(q_z - q_{hk}^z), \quad (4.18)$$

where $q_{hk}^r = 2\pi|k|/\lambda_r$. Thus, the scattering pattern in the ripple phase is a collection of Bragg rings for $k \neq 0$ centered at the meridian and the Bragg peaks for $k = 0$ located along the meridian. The scattering intensity is $I(\mathbf{q}) = |F(\mathbf{q})|^2 S(\mathbf{q})$, where $F(\mathbf{q})$ is the form factor. After the q_z integration, the observed, integrated intensity of (h, k) peak is proportional to

$$I_{hk}^{\text{obs}} \propto \frac{|F_{hk}|^2}{q_{hk}^z} \int dq_x \int_{-q_{hk}^{y0}}^{q_{hk}^{y0}} dq_y \frac{\delta(q_r - q_{hk}^r)}{2\pi q_r}, \quad (4.19)$$

where $q_{hk}^{y0} = \lambda(q_{hk}^z)^2/(4\pi)$. For side peaks ($k \neq 0$), we have

$$\begin{aligned} \int dq_x \int_{-q_{hk}^{y0}}^{q_{hk}^{y0}} dq_y \frac{\delta(q_r - q_{hk}^r)}{2\pi q_r} &\approx \int_{-q_{hk}^{y0}/q_{hk}^r}^{q_{hk}^{y0}/q_{hk}^r} d\phi \int dq_r q_r \frac{\delta(q_r - q_{hk}^r)}{2\pi q_r} \\ &= \frac{q_{hk}^{y0}}{\pi q_{hk}^r}. \end{aligned} \quad (4.20)$$

For main peaks ($k = 0$), we have

$$\begin{aligned} \int dq_x \int_{-q_{hk}^{y0}}^{q_{hk}^{y0}} dq_y \frac{\delta(q_r - q_{hk}^r)}{2\pi q_r} &= \int_0^{2\pi} d\phi \int dq_r q_r \frac{\delta(q_r - q_{hk}^r)}{2\pi q_r} \\ &= 1 \end{aligned} \quad (4.21)$$

Using Eq. (4.19 – 4.21), we write the observed integrated intensity as

$$I_{h0}^{\text{obs}} \propto \frac{|F_{h0}|^2}{q_{h0}^z} \quad (4.22)$$

$$I_{hk}^{\text{obs}} \propto \frac{|F_{hk}|^2}{q_{hk}^z} \frac{q_{hk}^{y0}}{\pi q_{hk}^r} = |F_{hk}|^2 \frac{\lambda q_{hk}^z}{2\pi} \frac{1}{2\pi q_{hk}^r} = |F_{hk}|^2 \frac{2\theta_{hk}}{2\pi q_{hk}^r}, \quad (4.23)$$

where $2\theta_{hk} = \lambda q_{hk}^z/(2\pi)$ is the incident angle at which the outgoing X-ray for the peak (h, k) is blocked by the substrate. Eq. (4.22) and (4.23) relate the form factor calculated from a model to the experimentally observed intensity, and are partially equivalent to Eq. (4.15) and (4.16).

In non-linear least squares fitting procedure, we fitted the observed integrated intensity to the calculated intensity from a bilayer model using these Lorentz corrections. This is because we can determine experimental uncertainties on observed intensity rather than the Lorentz-corrected form factors. We avoid propagating the uncertainties by fitting a model to observed intensity.

4.3.4 Absorption Correction for LAXS

In this section, we derive the absorption correction for the thin film sample. The calculation involves an explicit integration over the incident angle, ω , which is necessitated by the sample rotation during an x-ray exposure. The procedure is to write down an absorption factor, $A(\omega, \theta)$, for a given scattering angle at a given incident

angle, and then integrate over ω . We ignore q_x dependence because the X-ray path inside the sample is nearly within the y - z plane for low angle scattering. The correction for wide angle scattering is described in a later section.

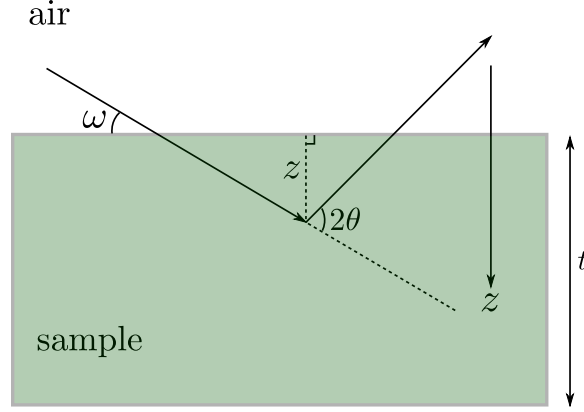


Figure 4.22: The path of X-rays within the sample. The incident angle is ω and the total scattering angle is 2θ . An X-ray with a penetration depth of z is shown. The total thickness of the sample is t .

Assume that all the X-rays enter the sample from the top surface. The total scattering angle is given by 2θ (see Fig. 4.22). Let z -axis point downward. At the top surface (air-sample interface), $z = 0$. For X-rays that travel to z and then scatter, the total path length within the sample is

$$L_{\text{tot}}(z, \omega, \theta) = \frac{z}{\sin \omega} + \frac{z}{\sin(2\theta - \omega)} = zg(\omega, \theta), \quad (4.24)$$

where $g(\omega, \theta) = (\sin \omega)^{-1} + (\sin(2\theta - \omega))^{-1}$. For each ray, the intensity is attenuated by the sample absorption. If non-attenuated intensity is equal to I_0 , then the attenuated intensity is

$$I(z, \omega, \theta) = I_0 \exp\left(-\frac{L_{\text{tot}}}{\mu}\right), \quad (4.25)$$

where μ is the absorption length of an X-ray. μ is 2.6 mm for 10.5 keV [79]. The observed intensity of scattering from a sample fixed at an angle ω is equal to the

integration of Eq. (4.25) over the total thickness of the sample and given by

$$\begin{aligned} I_{\text{obs}}(\omega, \theta) &= \int_0^t dz I(z, \omega, \theta) = I_0 \int_0^t dz \exp\left(-\frac{g(\omega, \theta)}{\mu} z\right) \\ &= I_0 \mu \frac{1 - \exp\left(-\frac{t}{\mu} g(\omega, \theta)\right)}{g(\omega, \theta)}. \end{aligned} \quad (4.26)$$

Defining the absorption factor at a fixed angle to be $A(\omega, \theta)$, the observed intensity can also be written as

$$I_{\text{obs}}(\omega, \theta) = A(\omega, \theta) t I_0, \quad (4.27)$$

where tI_0 is the intensity we would observe for non-absorbed X-rays. Equating Eq. (4.26) and (4.27), we get

$$A(\omega, \theta) = \frac{\mu}{t} \frac{1 - \exp\left(-\frac{t}{\mu} g(\omega, \theta)\right)}{g(\omega, \theta)}. \quad (4.28)$$

If μ is taken to infinity (no absorption), $A(\omega, \theta)$ goes to 1 as expected. The absorption factor A_{h0} for the $k = 0$ peaks is given by $A(\omega = \theta = \theta_B)$, plotted in Fig. 4.23. As shown, this factor is about 30 % for $h = 1$ peak, so it is not negligible.

For $k \neq 0$ side peaks, an integration over the incident angle ω is necessary because these peaks are observable at all our experimental incident angles as described in section 4.3.3. The total observed intensity from a rotating sample is simply

$$I_{\text{total}}(\theta) = \int_0^{2\theta} d\omega I_{\text{obs}}(\omega, \theta). \quad (4.29)$$

The upper integration limit is equal to 2θ because the substrate completely blocks the scattered X-rays above this angle as discussed in section 4.3.3. The total non-attenuated intensity is equal to $2\theta t I_0$. We, then, define the absorption factor $A(\theta)$ to be the ratio of the total observed intensity to the total non-attenuated intensity,

$$A(\theta) \equiv \frac{I_{\text{total}}(\theta)}{2\theta t I_0}. \quad (4.30)$$

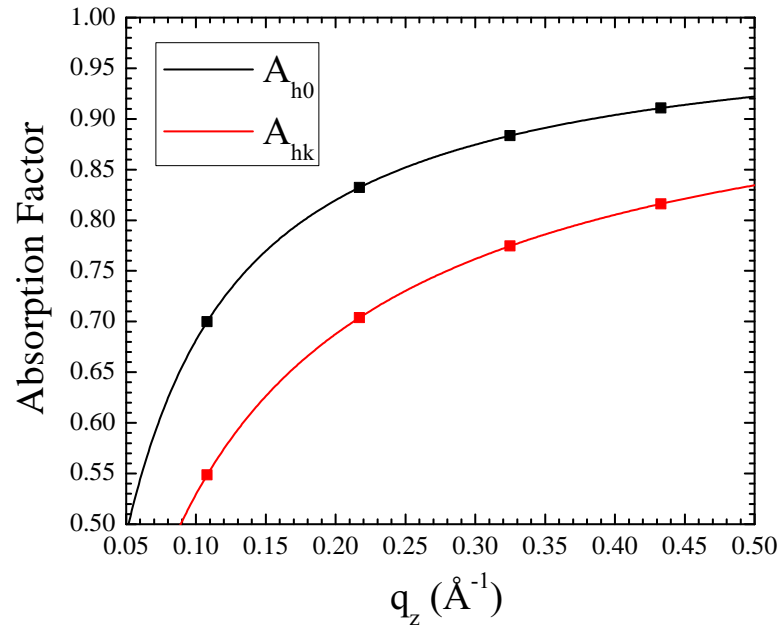


Figure 4.23: Absorption factors as a function of $q_z \approx 4\pi\theta/\lambda$. The values at $q_z = 2\pi h/D$ corresponding to $D = 58 \text{ \AA}$ are shown as squares. $\mu = 2600 \text{ }\mu\text{m}$, $t = 10 \text{ }\mu\text{m}$, and $\lambda = 1.175 \text{ \AA}$.

Using Eq. (4.28) and (4.29) in (4.30), we arrive at the final absorption factor

$$A(\theta) = \frac{1}{2\theta} \int_0^{2\theta} d\omega A(\omega, \theta) = \frac{\mu}{2\theta t} \int_0^{2\theta} d\omega \frac{1 - \exp\left(-\frac{t}{\mu} g(\omega, \theta)\right)}{g(\omega, \theta)}. \quad (4.31)$$

$A_{hk} = A(\theta)$ is plotted in Fig. 4.23. The absorption correction $A_c(\theta)$ is the inverse of Eq. (4.31).

4.3.5 Absorption Correction for WAXS

(Under construction)

4.3.6 Effect of mosaic spread

(Under construction)

4.4 Model

4.4.1 Contour Part of the Form Factor

As in Ref. [75], we take the ripple profile to have a sawtooth profile. Its amplitude is A and the projection of the major arm on the ripple direction is x_M as shown in Fig. 4.1. Then, we write the ripple profile as

$$u(x) = \begin{cases} -\frac{A}{\lambda_r - x_0} \left(x + \frac{\lambda_r}{2}\right) & \text{for } -\frac{\lambda_r}{2} \leq x < -\frac{x_0}{2}, \\ \frac{A}{x_0} x & \text{for } -\frac{x_0}{2} \leq x \leq \frac{x_0}{2}, \\ -\frac{A}{\lambda_r - x_0} \left(x - \frac{\lambda_r}{2}\right) & \text{for } \frac{x_0}{2} < x \leq \frac{\lambda_r}{2}. \end{cases} \quad (4.32)$$

The ripple profile has inversion symmetry, so that the resulting form factor is real. A and x_M are fitting parameters that depend on the integrated intensity of each peak while D , λ_r , and γ are determined from measuring the positions of the Bragg peaks.

In order to allow the electron density along the ripple direction to modulate, we include two additional parameters, one to allow for the electron density across the minor side to be different by a ratio f_1 from the electron density across the major side and a second parameter f_2 , which is multiplied by δ functions $\delta(x \pm x_M/2)$ to

allow for a different electron density near the kink between the major and the minor sides.

4.4.2 Transbilayer Part of the Form Factor

SDF

Delta function model is described here.

2G model

In the hybrid model, the terminal methyl region of the bilayer is represented as a Gaussian function [80]. The headgroups are represented by one and two Gaussian functions in 1G and 2G hybrid model, respectively. The methylene and water regions are each treated as a constant. The gap between the two constants is represented by a sine function. Then, for half of the bilayer, $0 \leq z \leq D/2$, the electron density has the form,

$$\rho(z) = \rho_G(z) + \rho_S(z) + \rho_B(z), \quad (4.33)$$

where the Gaussian part is given by

$$\rho_G(z) = \sum_{i=1}^{1 \text{ or } 2} \rho_{Hi} e^{-(z-Z_{Hi})^2/(2\sigma_{Hi}^2)} + \rho_M e^{-z^2/(2\sigma_M^2)}, \quad (4.34)$$

the strip part is given by

$$\rho_S(z) = \begin{cases} \rho_{CH_2} & \text{for } 0 \leq z < Z_{CH_2}, \\ \rho_W & \text{for } Z_W \leq z \leq D/2, \end{cases} \quad (4.35)$$

and the bridging part is given by

$$\rho_B(z) = \frac{\rho_W - \rho_{CH_2}}{2} \cos \left[\frac{-\pi}{\Delta Z_H} (z - Z_W) \right] + \frac{\rho_W + \rho_{CH_2}}{2} \quad \text{for } Z_{CH_2} < z < Z_W. \quad (4.36)$$

with $\Delta Z_H = Z_W - Z_{CH_2}$. Here, we assume $Z_{H2} > Z_{H1}$. Table 4.2 shows some of the definitions.

The transbilayer profile along $x = -z \tan \psi$ can be obtained by rotating the coordinates x and z by ψ in the clockwise direction and reexpressing $\rho(z)$ in terms of

	1G	2G
Z_{CH_2}	$Z_{\text{H1}} - \sigma_{\text{H1}}$	$Z_{\text{H1}} - \sigma_{\text{H1}}$
Z_{W}	$Z_{\text{H1}} + \sigma_{\text{H1}}$	$Z_{\text{H2}} + \sigma_{\text{H2}}$

Table 4.2: Definitions of Z_{CH_2} and Z_{W}

the rotated coordinates. This leads to replacing x with $x' = x \cos \psi + z \sin \psi$ and z with $z' = -x \sin \psi + z \cos \psi$. Then, the rotated transbilayer profile is

$$\rho(x, z) = \delta(x + z \tan \psi) [\rho_{\text{G}}(z') + \rho_{\text{S}}(z') + \rho_{\text{B}}(z')]. \quad (4.37)$$

Taking the two dimensional Fourier transform of Eq. (4.37) leads to the transbilayer part of the form factor,

$$F_{\text{T}} = \int_{-\frac{D}{2}}^{\frac{D}{2}} \int_{-\frac{\lambda_{\text{r}}}{2}}^{\frac{\lambda_{\text{r}}}{2}} [\rho(x, z) - \rho_{\text{W}}] e^{i(q_x x + q_z z)} dx dz \quad (4.38)$$

$$= F_{\text{G}} + F_{\text{S}} + F_{\text{B}}. \quad (4.39)$$

The form factor is calculated in the minus fluid convention, where the bilayer electron density is measured with respect to the electron density of the surrounding solvent. The expression for F_{T} is rather messy, so the derivation and full expression are in the appendix. Here, we note that the fitting parameters in this model are Z_{Hi} , σ_{Hi} , and R_{HiM} for each of the two headgroup Gaussian functions, σ_{M} for the terminal methyl Gaussian, ΔR for the methylene region, ψ for the lipid tilt, and an overall scaling factor. The contour part of the form factor has four more parameters (A , x_{M} , f_1 , and f_2). In total, the modified 2G hybrid model implements 14 structural parameters.

4.5 Results

4.5.1 Data and Electron Density Profile

Table 4.3 summarizes observed intensity from data shown in Fig. 4.5. We measured scattering on oriented samples in almost identical conditions as the best unoriented sample of Wack and Webb. As discussed earlier, these two types of samples have different Lorentz corrections, so this allowed us to check our data obtained on oriented samples against an unoriented sample.

h	k	I_{hk}^{obs}	box size	background
1	-1	??	??	??
1	0	??	??	??
1	1			
2	-1			
2	0			
2	1			

Table 4.3: Observed intensity

Show a table showing our measured form factor (Lorentz corrected). Do the fits once we decide on mosaic spread correction. Show in a table, fitting results. Show an edp. Show the thicknesses of both arms. Comment on some fine features.

4.5.2 Near Grazing Incidence Wide Angle X-ray Scattering (NGIWAXS)

Figure 4.24 shows near grazing incidence Wide Angle X-ray scattering (NGIWAXS) from an oriented DMPC film in the ripple phase. As can be seen, hydrocarbon chain scattering did not vary considerably between the two D -spacings. A weak feature that looks like an arc coming from the chain peak was observed. This feature extended out from $\phi = 0^\circ$ to at least 70° . This feature might simply be mosaic spread scattering due to the peak near the equator. Because mosaic spread of this sample was very small, it may also be possible that the feature is not mosaic spread arc, but comes from the minor arm, indicating that tilt modulation may occur in the minor arm. Chains are packed quite tightly, unlike in the fluid phase. (I did rocking scan, so show the data, and maybe estimate what scattering would look like based on Lorentzian distribution.)

Figure 4.25 shows an enlarged image of the ripple phase WAXS at $D = 60.8 \text{ \AA}$. We observed a strong peak off the equator and a weak one, the center of which was not determined. The maximum intensity of the strong peak was at $(q_r, q_z) \approx (1.49 \text{ \AA}^{-1}, 0.19 \text{ \AA}^{-1})$ as shown in Fig. 4.26. The weak peak was observed near the equator, but separation of this peak from the strong one was most visible at $q_z = 0.13 \text{ \AA}^{-1}$ as Fig. 4.26 shows. Separation of the two peaks was possible because of the high resolution experiment. In previous runs with the low resolution setup, the ripple peak appeared as a single wide peak.

(some thought) Can we say that the observed arc like scattering is not the mosaic spread, but true sample scattering? Comment on the widths of the peaks observed. Possibly make use of both low and high resolution data. Apply the absorption correction. Show q swaths for various ϕ .

4.5.3 Transmission WAXS

Convert the image to q -space. No strong order on the equator. Compare to NGIWAXS and comment on the absorption effect in NGIWAXS data.

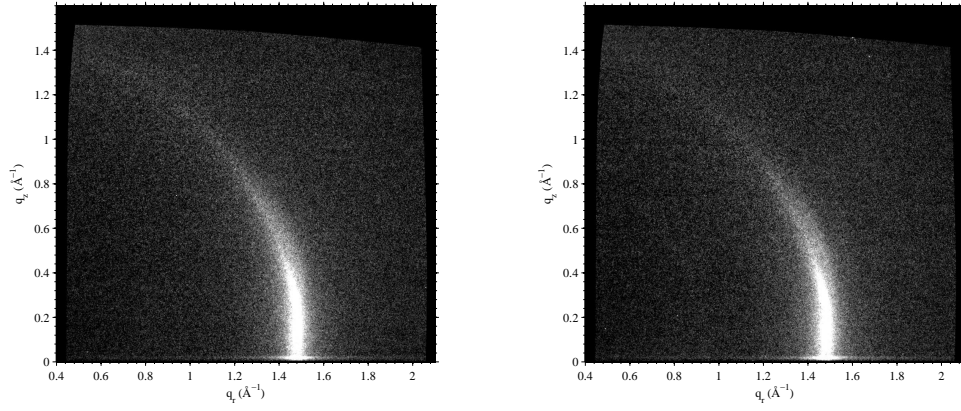


Figure 4.24: NGIWAXS of the DMPC ripple phase for $D = 59.2 \text{ \AA}$ (left) and 60.8 \AA (right). The angle of incidence ω was 0.2° . The black regions around the edge of each image are the q -space that was not probed. The distorted, non rectangular shape of the probed q -space signifies non-linear relation between the CCD space and sample q -space.

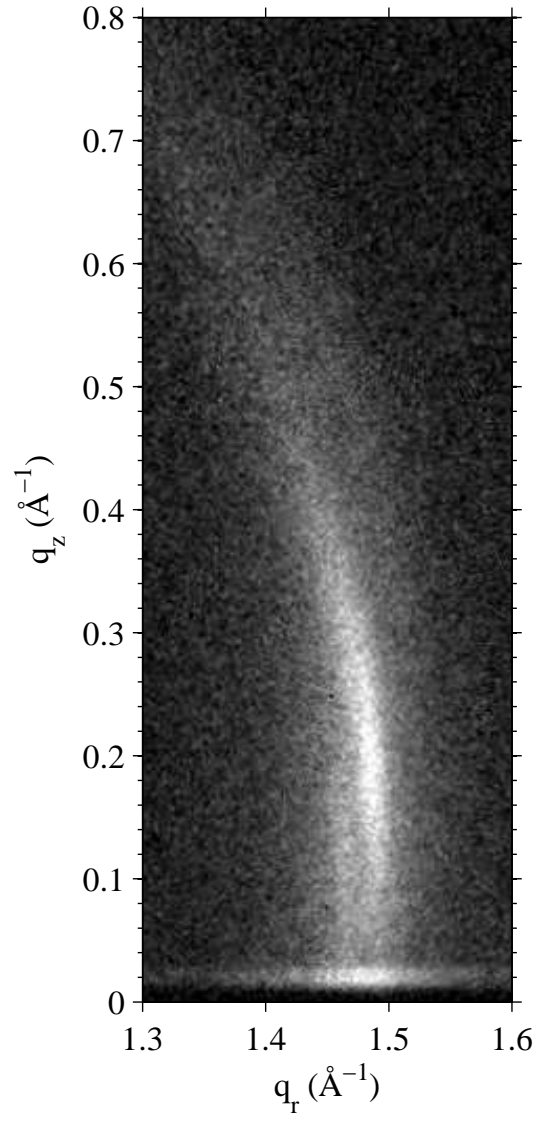


Figure 4.25: Enlarged view of the right image in Fig. 4.24. To show smaller features around the peak, a different contrast is used.

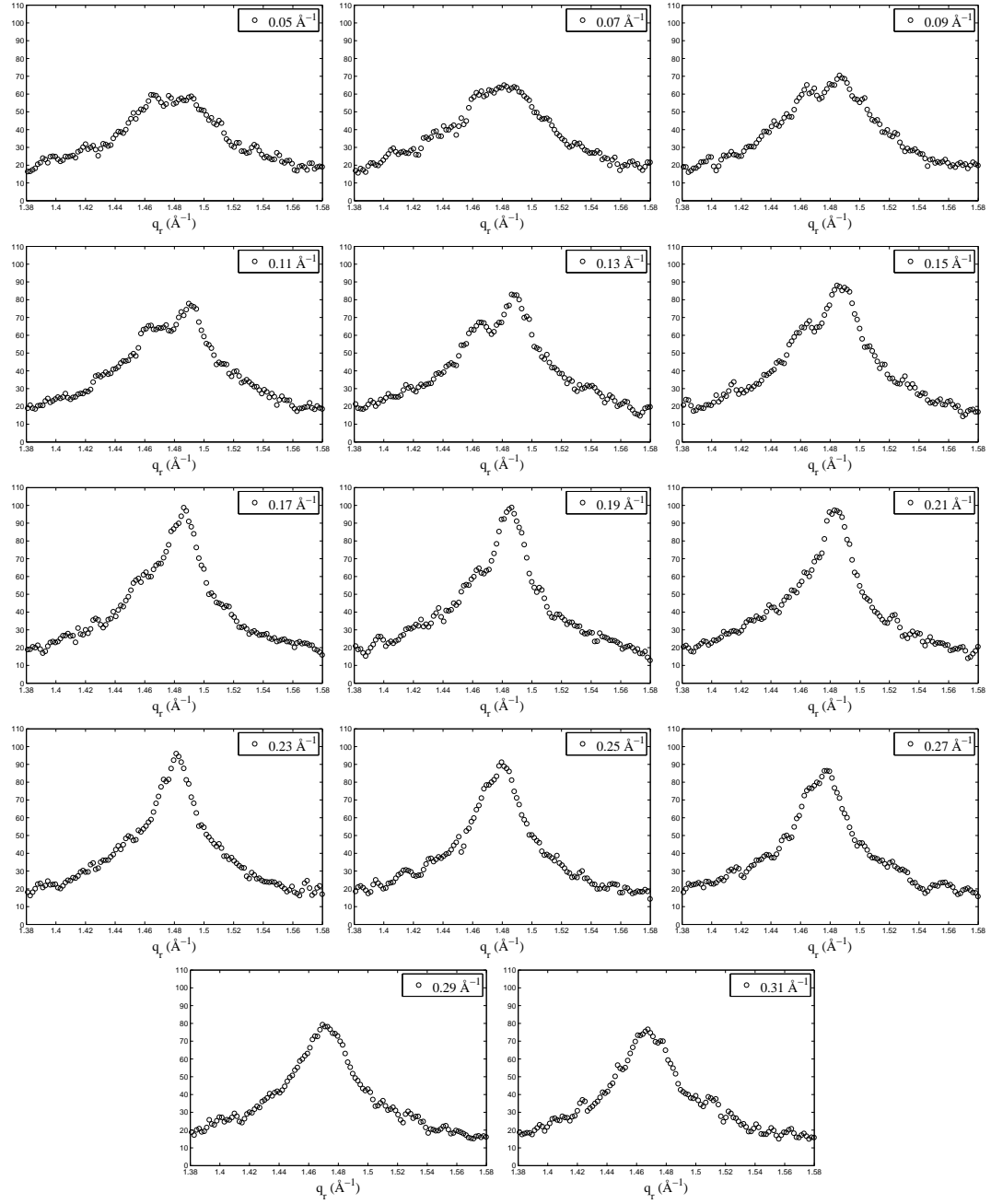


Figure 4.26: q_r swaths, each averaged over 0.02\AA^{-1} . The center q_z value of a swatch is shown in the figure legends.

4.6 Discussion

Comparison with previous unoriented/oriented stuff.

4.7 Conclusion

Future possible experiments include the high resolution transmission experiment, where both geometric broadening and energy dispersion are minimized. The expected resolution is the width of the X-ray beam, which is about 3 pixels. This experiment doubles the best resolution achieved in this work. Another slightly different high resolution experiment is to use silicon crystal analyzer downstream of the sample, which completely remove geometric broadening. The downside of this type of high resolution experiment is that only one point in q -space is probed at any given exposure, so to get a full 2D map of wide angle scattering is time consuming.

Appendices

Appendix A

Tat

A.1 Analysis of Fixed Angle Data using NFIT

In this section, I propose a slightly new method to analyze the diffuse scattering data. This method may allow us to measure the X-ray form factor at lower q_z than we have traditionally measured.

A.1.1 Theory

A.1.2 Results

A.2 Mosaic Spread for NFIT analysis

First we describe an analysis of mosaic spread for diffuse scattering. Next we discuss some experimental methods. Third, we discuss the updated NFIT program. Fourth, we show the results.

A.2.1 Mosaic Spread: Calculation

In this section, an analytical framework for dealing with mosaic spread is developed. A sample of oriented stacks of bilayers consists of many small domains, within which layers are registered in an array. The stacking direction \mathbf{n}' of a domain is the direction perpendicular to these layers. A “perfect” domain is a domain parallel to the substrate xy -plane and its stacking direction is \mathbf{n} as shown in Fig. A.1. Then, we consider a mosaic spread distribution function, $P(\alpha)$, representing a probability of finding a

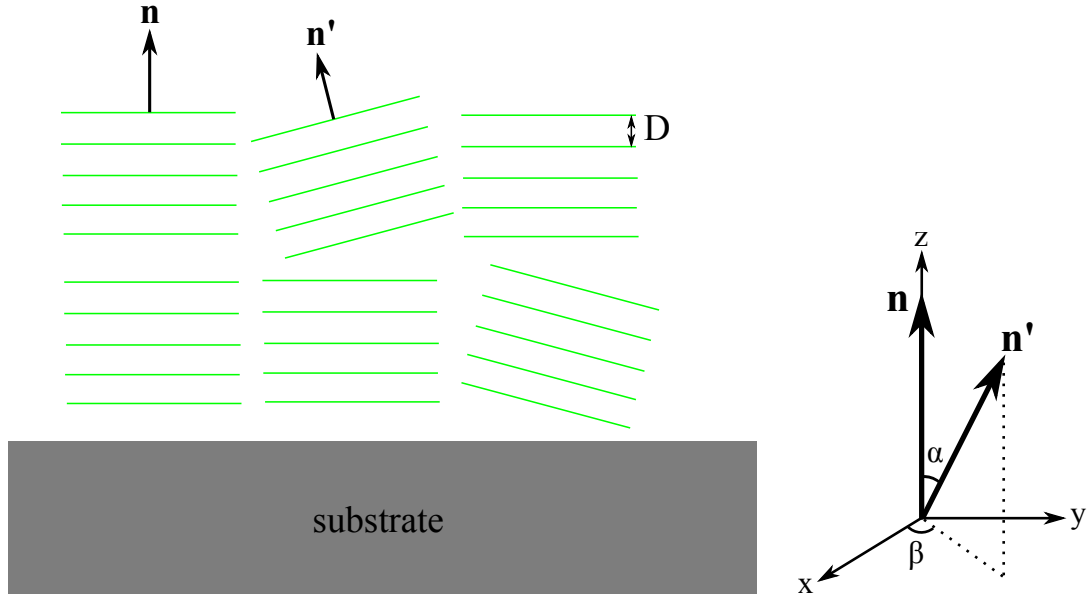


Figure A.1: Two dimensional view of mosaic spread (left) and notations used in this section (right). The stacking direction of a perfect domain is \mathbf{n} and that of a tilted domain \mathbf{n}' . The deviation of \mathbf{n}' from \mathbf{n} denoted as α quantifies the degree of mis-orientation of a domain. The x , y , and z -axes are the sample coordinates.

domain with tilt α . We assume that the sample is symmetric about the substrate normal \mathbf{n} , so that the distribution $P(\alpha)$ does not depend on the azimuthal angle, β . The normalization condition on $P(\alpha)$ is

$$1 = \int_0^{2\pi} d\beta \int_0^{\frac{\pi}{2}} d\alpha \sin \alpha P(\alpha). \quad (\text{A.1})$$

The object of this section is to derive the X-ray scattering structure factor including the distribution function $P(\alpha)$.

First, let us consider a two dimensional example. Our sample consists of two identical domains except a tilt α shown in Fig. A.2. Then, the sample structure factor $S^{\text{sam}}(\mathbf{q})$ is a superposition of the structure factor $S(\mathbf{q})$ of the perfect domain and $S(\mathbf{q}')$ of the tilted domain,

$$S^{\text{sam}}(\mathbf{q}) = S(q_x, q_z) + S(q'_x, q'_z). \quad (\text{A.2})$$

To express $S(q'_x, q'_z)$ in terms of the sample q -space (q_x, q_z) , we write q'_x and q'_z in

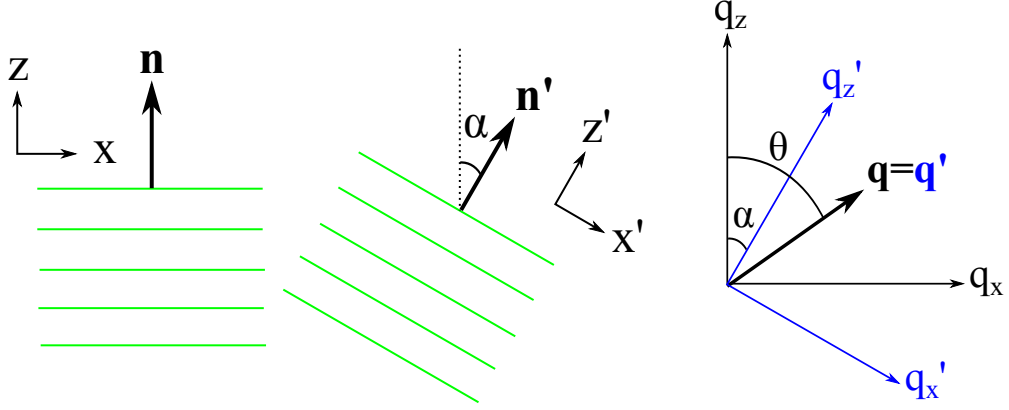


Figure A.2: Example of a two dimensional sample consisting of a perfect and tilted domains. $\mathbf{q} = (q_x, q_z)$ is the sample q -space and $\mathbf{q}' = (q'_x, q'_z)$ is the domain q -space. The two q -spaces are related by a rotation of α about the y -axis, which is into the page.

terms of q_x , q_z , and α ,

$$\begin{aligned}
 q'_x &= \mathbf{q} \cdot \hat{\mathbf{x}}' = q \cos\left(\frac{\pi}{2} - \theta + \alpha\right) \\
 q'_z &= \mathbf{q} \cdot \hat{\mathbf{z}}' = q \sin\left(\frac{\pi}{2} - \theta + \alpha\right) \\
 q_x &= q \cos(\pi/2 - \theta) \\
 q_z &= q \sin(\pi/2 - \theta)
 \end{aligned} \tag{A.3}$$

where $q = |\mathbf{q}|$. Eq. (A.2) and (A.3) give the structure factor of a sample consisting of the two domains. With a continuous distribution of \mathbf{n}' , we integrate over the angle α with each structure factor modulated by the distribution function $P(\alpha)$,

$$S_M(\mathbf{q}) = S_M(q, \theta) = \int_{-\pi/2}^{\pi/2} d\alpha S(q'_x, q'_z) P(\alpha), \tag{A.4}$$

Variables q and θ are used in the above equation to make a connection with the three dimensional case, where the spherical coordinates are convenient, which we discuss now.

For a three dimensional sample, the basic idea is the same as the two dimensional case. In the three dimensional case, we also rotate the vector about the z -axis by an angle β after the rotation about the y -axis by an angle α , so all we need to do is to apply appropriate rotation matrices to the sample xyz -axes, which, then, defines the

domain coordinates $x'y'z'$.

The rotation matrix for rotating a vector about y-axis is given by

$$\begin{pmatrix} \cos \alpha & 0 & -\sin \alpha \\ 0 & 1 & 0 \\ \sin \alpha & 0 & \cos \alpha \end{pmatrix} \quad (\text{A.5})$$

and for rotating about z-axis

$$\begin{pmatrix} \cos \beta & \sin \beta & 0 \\ -\sin \beta & \cos \beta & 0 \\ 0 & 0 & 1 \end{pmatrix}. \quad (\text{A.6})$$

Then, what we want is

$$\hat{\mathbf{x}}' = \begin{pmatrix} \cos \beta & \sin \beta & 0 \\ -\sin \beta & \cos \beta & 0 \\ 0 & 0 & 1 \end{pmatrix} \begin{pmatrix} \cos \alpha & 0 & -\sin \alpha \\ 0 & 1 & 0 \\ \sin \alpha & 0 & \cos \alpha \end{pmatrix} \begin{pmatrix} 1 \\ 0 \\ 0 \end{pmatrix} = \begin{pmatrix} \cos \alpha \cos \beta \\ \cos \alpha \sin \beta \\ -\sin \alpha \end{pmatrix} \quad (\text{A.7})$$

$$\hat{\mathbf{y}}' = \begin{pmatrix} \cos \beta & \sin \beta & 0 \\ -\sin \beta & \cos \beta & 0 \\ 0 & 0 & 1 \end{pmatrix} \begin{pmatrix} \cos \alpha & 0 & -\sin \alpha \\ 0 & 1 & 0 \\ \sin \alpha & 0 & \cos \alpha \end{pmatrix} \begin{pmatrix} 0 \\ 1 \\ 0 \end{pmatrix} = \begin{pmatrix} -\sin \beta \\ \cos \beta \\ 0 \end{pmatrix} \quad (\text{A.8})$$

$$\hat{\mathbf{z}}' = \begin{pmatrix} \cos \beta & \sin \beta & 0 \\ -\sin \beta & \cos \beta & 0 \\ 0 & 0 & 1 \end{pmatrix} \begin{pmatrix} \cos \alpha & 0 & -\sin \alpha \\ 0 & 1 & 0 \\ \sin \alpha & 0 & \cos \alpha \end{pmatrix} \begin{pmatrix} 0 \\ 0 \\ 1 \end{pmatrix} = \begin{pmatrix} \sin \alpha \cos \beta \\ \sin \alpha \sin \beta \\ \cos \alpha \end{pmatrix}. \quad (\text{A.9})$$

The domain q -space, (q'_x, q'_y, q'_z) , in terms of the sample q -space (q_x, q_y, q_z) is given by

$$q'_x = \mathbf{q} \cdot \hat{\mathbf{x}}' = q_x \cos \alpha \cos \beta + q_y \cos \alpha \sin \beta - q_z \sin \alpha, \quad (\text{A.10})$$

$$q'_y = \mathbf{q} \cdot \hat{\mathbf{y}}' = -q_x \sin \beta + q_y \cos \beta, \quad (\text{A.11})$$

$$q'_z = \mathbf{q} \cdot \hat{\mathbf{z}}' = q_x \sin \alpha \cos \beta + q_y \sin \alpha \sin \beta + q_z \cos \alpha. \quad (\text{A.12})$$

The transformation expressed in the spherical coordinates is

$$\cos \theta' = \frac{q'_z}{q} = \sin \theta \sin \alpha \cos(\phi - \beta) + \cos \theta \cos \alpha, \quad (\text{A.13})$$

$$\tan \phi' = \frac{q'_y}{q'_x} = \frac{\sin \theta \sin(\phi - \beta)}{\sin \theta \cos \alpha \cos(\phi - \beta) - \cos \theta \sin \alpha}. \quad (\text{A.14})$$

Summing over all the domains, we get for the mosaic spread modified structure factor

$$S_M(q, \theta, \phi) = \int_0^{2\pi} d\beta \int_0^{\frac{\pi}{2}} d\alpha S(q, \theta', \phi') P(\alpha) \quad (\text{A.15})$$

with Eq. (A.13) and Eq. (A.14).

The structure factor for a stack of rigid layers with their normals parallel to the z -axis in the spherical coordinates is

$$S(q, \theta, \phi) = \frac{\delta(q - \frac{2\pi h}{D})}{q^2} \delta(\cos \theta - 1) \delta(\phi) \quad (\text{A.16})$$

where $\delta(x)$ is the Dirac delta function. From Eq. (A.14), $\delta(\phi')$ is equivalent to $\delta(\beta - \phi)$. Setting $\beta = \phi$ in Eq. (A.13) gives $\cos \theta' = \cos(\alpha - \theta)$. Then, the mosaic spread modified structure factor $S_M(\mathbf{q})$ is

$$\begin{aligned} S_M(q, \theta, \phi) &= \int d\alpha \int d\beta \frac{\delta(q - \frac{2\pi h}{D})}{q^2} \delta(\cos \theta' - 1) \delta(\beta - \phi) P(\alpha) \\ &= \frac{\delta(q - \frac{2\pi h}{D})}{q^2} \int d\alpha \delta(\cos[\alpha - \theta] - 1) P(\alpha) \\ &= \frac{\delta(q - \frac{2\pi h}{D})}{q^2} P(\theta). \end{aligned} \quad (\text{A.17})$$

Eq. (A.17) suggests a hemispherical shell of intensity with a radius of $2\pi h/D$ in the sample q -space. As will be described in the next section, a 2D detector records a cross section of this shell, which gives rise to mosaic arcs along $q = 2\pi h/D$.

A.2.2 Mosaic Spread: Experiment

(Under construction) In this section, we discuss experimental procedures to probe appropriate q -space to measure the mosaic distribution, $P(\alpha)$. In our setup, the angle of incidence between the beam and substrate, denoted by ω , can be varied. A

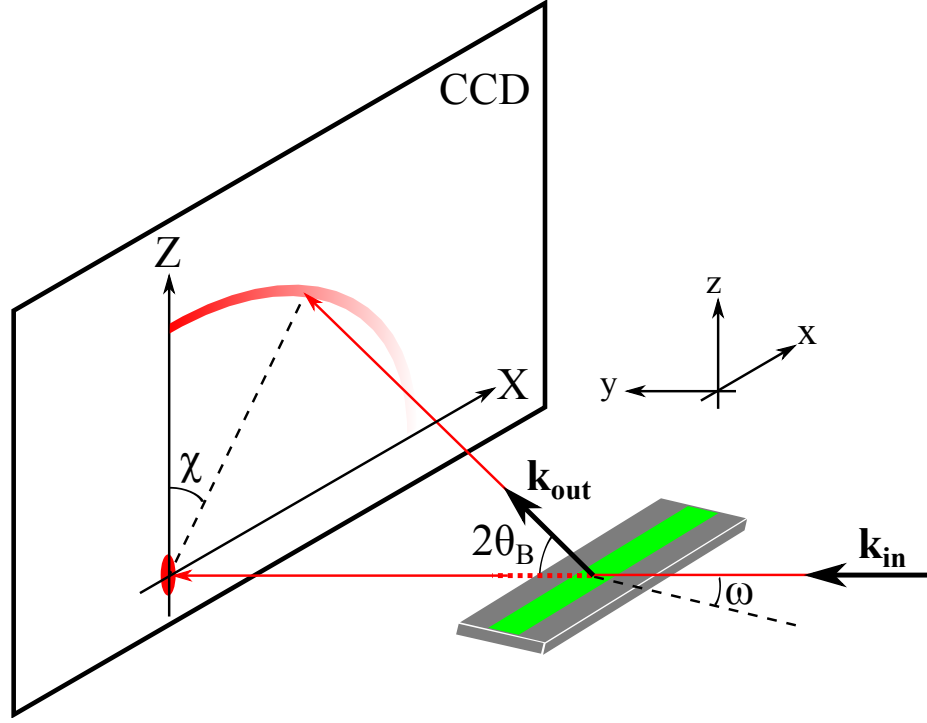


Figure A.3: Notations used in this section. The arc originating from the Z -axis is the mosaic arc due to the mosaic spread distribution.

conventional method to measure mosaicity distribution is a rocking scan, where one measures the integrated intensity of a given Bragg peak as a function of ω with a fixed detector position. Another method called ring analysis measures the intensity as a function of χ on a two dimensional detector (see Fig. A.3). First, we want to compare the two methods mentioned above and figure out the exact relationship between them.

Using the coordinates defined in Fig. A.3, borrowing Eq. (4.12), and replacing $\phi = \pi/2 - \chi$, we have

$$\begin{aligned}
 q_x &= q \cos \theta \sin \chi, \\
 q_y &= q (-\sin \theta \cos \omega + \cos \theta \cos \chi \sin \omega), \\
 q_z &= q (\sin \theta \sin \omega + \cos \theta \cos \chi \cos \omega),
 \end{aligned} \tag{A.18}$$

or in the small angle approximation,

$$\begin{aligned}
q_x &\approx \frac{4\pi\theta \sin \chi}{\lambda} \approx kX/S \\
q_y &\approx q_z\omega - \frac{4\pi\theta^2}{\lambda} \approx q_z\omega - \frac{\lambda q_z^2}{4\pi} \\
q_z &\approx \frac{4\pi\theta \cos \chi}{\lambda} \approx kZ/S.
\end{aligned} \tag{A.19}$$

For a rocking scan focused on a particular order, $\chi = 0$ and $\theta = \theta_B$ while ω is varied about θ_B , where θ_B is the Bragg angle. Then,

$$\begin{aligned}
q_x &= 0 \\
q_y &= q \sin(\omega - \theta_B) \\
q_z &= q \cos(\omega - \theta_B),
\end{aligned} \tag{A.20}$$

which shows that this scan traces a part of the circular path in the $q_x = 0$ plane as shown in Fig. A.4. As Fig. A.4 shows, however, the rocking scan only probes a small fraction of the entire distribution, limited by $2\theta_B$. As discussed in section 4.3.3, beyond $\omega = 2\theta_B$, the substrate blocks scattering. On the other hand, the ring analysis takes an advantage of a two dimensional detector and can probe a substantially wider range of the distribution, approximately $\pm 45^\circ$ at $\omega = \theta_B$. This method is now described.

In the ring method, we set $\omega = \theta_B$ and scan on the detector along $\theta = \theta_B$ as a function of χ . Then, Eq. (A.18) becomes

$$\begin{aligned}
q_x &= q \cos \theta_B \sin \chi, \\
q_y &= q \sin \theta_B \cos \theta_B (\cos \chi - 1), \\
q_z &= q(\sin^2 \theta_B + \cos^2 \theta_B \cos \chi),
\end{aligned} \tag{A.21}$$

where $q = 4\pi \sin \theta_B / \lambda$. For small θ_B , Eq. (A.21) is reduced to

$$\begin{aligned}
q_x &\approx q \sin \chi, \\
q_y &\approx 0, \\
q_z &\approx q \cos \chi.
\end{aligned} \tag{A.22}$$

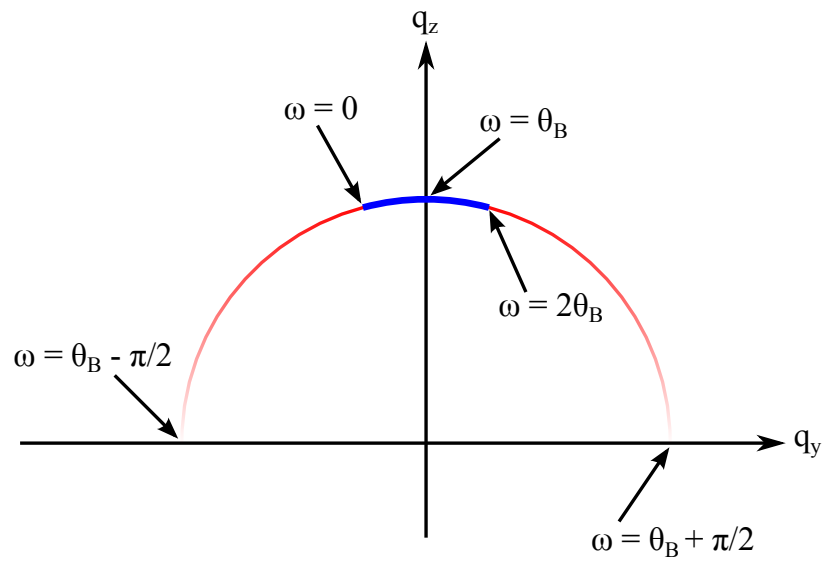


Figure A.4: Rocking scan trace in q -space.

Thus, the rocking scan and ring analysis are equivalent for small θ_B , the condition of which is satisfied for low angle X-ray scattering.

A.2.3 NFIT

The updated NFIT first calculates a theoretical structure factor in cylindrical coordinates [37]. This calculated structure factor $S(q_r, q_z)$ has rotational symmetry about the z -axis, which eliminates ϕ' dependence in Eq. (A.15). The program interpolates $S(q_r, q_z)$ in terms of the spherical coordinates q and θ with $\phi = 0$ to perform the double integration in Eq. (A.15). After the mosaic spread integration, q_y integration is done. For this integration, the calculated S_M is interpolated in terms of q_x , q_y , and q_z .

If the structure factor defined in the Cartesian coordinates are desired (for a case of square domains instead of circular ones), Eq. (A.10 – A.12) can be used instead of Eq. (A.13) and (A.14).

An issue with the current analysis comes from the form factor $|F(q_z)|$, which is not calculated from a model in the NFIT. Because the mosaic spread integration mixes up intensity at different q_z values, the separation of $|F(q_z)|$ from $S(\mathbf{q})$ is in principle impossible. One way to deal with this issue is to combine the SDP and NFIT programs, but that will end up with too many non-linear parameters. Another way to deal is to limit the fitting range to regions close to the meridian and truncate the distribution at an angle much smaller than $\pi/2$. For a small range of integration, it is not unreasonable to assume that the form factor is approximately constant as can be seen from Eq. (A.12) with small q_x , q_y , and α . Therefore, the analysis developed in this appendix ignores the form factor.

A.2.4 Results

A.3 Some More Details of Tat Stuff if needed

Appendix B

Ripple Phase

B.1 Derivation of the contour part of the form factor

In this section, we derive F_C . The ripple profile, $u(x)$ is given by

$$u(x) = \begin{cases} -\frac{A}{\lambda_r - x_0} \left(x + \frac{\lambda_r}{2}\right) & \text{for } -\frac{\lambda_r}{2} \leq x < -\frac{x_0}{2} \\ \frac{A}{x_0} x & \text{for } -\frac{x_0}{2} \leq x \leq \frac{x_0}{2} \\ -\frac{A}{\lambda_r - x_0} \left(x - \frac{\lambda_r}{2}\right) & \text{for } \frac{x_0}{2} < x \leq \frac{\lambda_r}{2} \end{cases} \quad (\text{B.1})$$

The contour part of the form factor is the Fourier transform of the contour function, $C(x, z)$,

$$F_C(\mathbf{q}) = \frac{1}{\lambda_r} \int_{-\frac{\lambda_r}{2}}^{\frac{\lambda_r}{2}} dx \int_{-\frac{D}{2}}^{\frac{D}{2}} dz C(x, z) e^{iq_z z} e^{iq_x x}$$

As discussed in section X, the modulated models allow the electron density to modulate along the ripple direction, x . This means

$$C(x, z) = \begin{cases} f_1 \delta[z - u(x)] & \text{for } -\frac{\lambda_r}{2} \leq x < -\frac{x_0}{2} \\ \delta[z - u(x)] & \text{for } -\frac{x_0}{2} < x < \frac{x_0}{2} \\ f_1 \delta[z - u(x)] & \text{for } \frac{x_0}{2} \leq x < \frac{\lambda_r}{2} \end{cases} + f_2 \delta\left(x + \frac{x_0}{2}\right) \delta\left(z + \frac{A}{2}\right) + f_2 \delta\left(x - \frac{x_0}{2}\right) \delta\left(z - \frac{A}{2}\right). \quad (\text{B.2})$$

The contribution from the minor arm is

$$\begin{aligned}
& \frac{1}{\lambda_r} \int_{-\frac{\lambda_r}{2}}^{-\frac{x_0}{2}} dx e^{iq_x x} e^{iq_z u(x)} + \int_{\frac{x_0}{2}}^{\frac{\lambda_r}{2}} dx e^{iq_x x} e^{iq_z u(x)} \\
&= \frac{1}{\lambda_r} \int_{\frac{x_0}{2}}^{\frac{\lambda_r}{2}} dx e^{-i \left[q_x x - q_z \frac{A}{\lambda_r - x_0} \left(x - \frac{\lambda_r}{2} \right) \right]} + \int_{\frac{x_0}{2}}^{\frac{\lambda_r}{2}} dx e^{i \left[q_x x - q_z \frac{A}{\lambda_r - x_0} \left(x - \frac{\lambda_r}{2} \right) \right]} \\
&= \frac{2}{\lambda_r} \int_{\frac{x_0}{2}}^{\frac{\lambda_r}{2}} \cos \left[\left(q_x - q_z \frac{A}{\lambda_r - x_0} \right) x + q_z \frac{A}{\lambda_r - x_0} \frac{\lambda_r}{2} \right] dx
\end{aligned} \tag{B.3}$$

Using a trigonometric identity,

$$\sin u - \sin v = 2 \cos[(u + v)/2] \sin[(u - v)/2],$$

and defining

$$\omega(\mathbf{q}) = \frac{1}{2} (q_x x_0 + q_z A), \tag{B.4}$$

we further simplify Eq. (B.3),

$$\begin{aligned}
&= \frac{2}{\lambda_r} \frac{\lambda_r - x_0}{\frac{1}{2} q_x \lambda_r - \omega} \cos \left[\frac{1}{2} \left(\frac{1}{2} q_x \lambda_r + \omega \right) \right] \sin \left[\frac{1}{2} \left(\frac{1}{2} q_x \lambda_r - \omega \right) \right] \\
&= \frac{1}{\lambda_r} \frac{\lambda_r - x_0}{\frac{1}{2} q_x \lambda_r - \omega} \cos \left[\frac{1}{2} \left(\frac{1}{2} q_x \lambda_r + \omega \right) \right] \frac{\sin \left(\frac{1}{2} q_x \lambda_r - \omega \right)}{\cos \left[\frac{1}{2} \left(\frac{1}{2} q_x \lambda_r - \omega \right) \right]} \\
&= \frac{\lambda_r - x_0}{\lambda_r} \frac{\cos \left[\frac{1}{2} \left(\frac{1}{2} q_x \lambda_r + \omega \right) \right] \sin \left(\frac{1}{2} q_x \lambda_r - \omega \right)}{\cos \left[\frac{1}{2} \left(\frac{1}{2} q_x \lambda_r - \omega \right) \right] \frac{1}{2} q_x \lambda_r - \omega}.
\end{aligned} \tag{B.5}$$

Similarly, we calculate the contribution from the major arm,

$$\begin{aligned}
\frac{1}{\lambda_r} \int_{-\frac{x_0}{2}}^{\frac{x_0}{2}} dx e^{i \left(\frac{q_z A}{x_0} + q_x \right) x} &= \frac{2}{\lambda_r} \int_0^{\frac{x_0}{2}} dx \cos \left(\frac{q_z A}{x_0} + q_x \right) x \\
&= \frac{x_0}{\lambda_r} \frac{\sin \omega}{\omega}
\end{aligned} \tag{B.6}$$

The contribution from the kink region is

$$\begin{aligned}
& \frac{1}{\lambda_r} \iint dx dz \left[\delta \left(x + \frac{x_0}{2} \right) \delta \left(z + \frac{A}{2} \right) + \delta \left(x - \frac{x_0}{2} \right) \delta \left(z - \frac{A}{2} \right) \right] e^{iq_x x} e^{iq_z z} \\
&= \frac{2}{\lambda_r} \cos \omega.
\end{aligned} \tag{B.7}$$

Therefore,

$$F_C(\mathbf{q}) = \frac{x_0}{\lambda_r} \frac{\sin \omega}{\omega} + f_1 \frac{\lambda_r - x_0}{\lambda_r} \frac{\cos \left[\frac{1}{2} \left(\frac{1}{2} q_x \lambda_r + \omega \right) \right]}{\cos \left[\frac{1}{2} \left(\frac{1}{2} q_x \lambda_r - \omega \right) \right]} \frac{\sin \left(\frac{1}{2} q_x \lambda_r - \omega \right)}{\frac{1}{2} q_x \lambda_r - \omega} + \frac{2f_2}{\lambda_r} \cos \omega \quad (\text{B.8})$$

B.2 Rotation of a Two-Dimensional Function

Let us consider rotating a function, $f(x, z)$ in two dimensions by an angle, ψ , in the counterclockwise direction (see Fig. X). This is easily achieved by rotating the coordinate system by ψ in the clockwise direction. Let rotated coordinates be x' and z' . A point in the original coordinates, (x, z) , is written as (x', z') in the new coordinates. More specifically, the point \mathbf{P} is written as $\mathbf{P} = x\hat{\mathbf{x}} + z\hat{\mathbf{z}} = x'\hat{\mathbf{x}}' + z'\hat{\mathbf{z}}'$. $\hat{\mathbf{x}}$ and $\hat{\mathbf{z}}$ in the $x'z'$ coordinate system are written as

$$\hat{\mathbf{x}} = \cos \psi \hat{\mathbf{x}}' + \sin \psi \hat{\mathbf{z}}' \quad (\text{B.9})$$

$$\hat{\mathbf{z}} = -\sin \psi \hat{\mathbf{x}}' + \cos \psi \hat{\mathbf{z}}'. \quad (\text{B.10})$$

Plugging these in $\mathbf{P} = x\hat{\mathbf{x}} + z\hat{\mathbf{z}}$ leads to

$$x' = x \cos \psi - z \sin \psi \quad (\text{B.11})$$

$$z' = z \cos \psi + x \sin \psi, \quad (\text{B.12})$$

the inverse of which is

$$x = x' \cos \psi + z' \sin \psi \quad (\text{B.13})$$

$$z = -x' \sin \psi + z' \cos \psi. \quad (\text{B.14})$$

Using the latter equations, $f(x, z)$ can be expressed in terms of x' and z' . The resulting function $f(x', z')$ is the rotated version of $f(x, z)$.

As an example, let us consider a Dirac delta function located at $(x, z) = (0, Z_H)$,

that is, $f(x, z) = \delta(x)\delta(z - Z_{\text{H}})$. After the rotation by ψ , it becomes

$$\begin{aligned}
f(x, z) &\rightarrow \delta(x \cos \psi + z \sin \psi) \delta(-x \sin \psi + z \cos \psi - Z_{\text{H}}) \\
&= \frac{\delta(x + z \tan \psi)}{|\cos \psi|} \frac{\delta(-x \sin \psi \cos \psi + z \cos^2 \psi - Z_{\text{H}} \cos \psi)}{1/|\cos \psi|} \\
&= \delta(x + z \tan \psi) \delta(z \tan \psi \sin \psi \cos \psi + z \cos^2 \psi - Z_{\text{H}} \cos \psi) \\
&= \delta(x + z \tan \psi) \delta(z - Z_{\text{H}} \cos \psi),
\end{aligned}$$

which is a part of the expression for $T_\psi(x, z)$ in the simple delta function model.

B.3 Derivation of the transbilayer part of the form factor in the 2G hybrid model

In this section, we derive the trasbilayer part of the form factor calculated from the 2G hybrid model discussed in section X. Defining $z' = -x \sin \psi + z \cos \psi$, the Fourier transform of a Gaussian function along the line tilted from z -axis by ψ is

$$\begin{aligned}
&\iint dz dx \rho_{\text{Hi}} \exp\left\{-\frac{(z' - Z_{\text{Hi}})^2}{2\sigma_{\text{Hi}}^2}\right\} \delta(x \cos \psi + z \sin \psi) e^{iq_x x} e^{iq_z z} \\
&= \frac{1}{\cos \psi} \int_{-\frac{D}{2}}^{\frac{D}{2}} dz \rho_{\text{Hi}} \exp\left\{-\frac{(z - Z_{\text{Hi}} \cos \psi)^2}{2\sigma_{\text{Hi}}^2 \cos^2 \psi} + i(q_z - q_x \tan \psi)z\right\} \\
&\approx \rho_{\text{Hi}} \sqrt{2\pi} \sigma_{\text{Hi}} \exp\left\{i\alpha Z_{\text{Hi}} - \frac{1}{2}\alpha^2 \sigma_{\text{Hi}}^2\right\}
\end{aligned} \tag{B.15}$$

with $\alpha = q_z \cos \psi - q_x \sin \psi$. Using Eq. (B.15) and adding the other side of the bilayer and the terminal methyl term, we get

$$\begin{aligned}
F_{\text{G}} = \sqrt{2\pi} \left[-\rho_{\text{M}} \sigma_{\text{M}} \exp\left\{-\frac{1}{2}\alpha^2 \sigma_{\text{M}}^2\right\} \right. \\
\left. + \sum_{i=1}^{1 \text{ or } 2} 2\rho_{\text{Hi}} \sigma_{\text{Hi}} \cos(\alpha Z_{\text{Hi}}) \exp\left\{-\frac{1}{2}\alpha^2 \sigma_{\text{Hi}}^2\right\} \right]. \tag{B.16}
\end{aligned}$$

The strip part of the model in the minus fluid convention is

$$\rho_S(z) = \begin{cases} -\Delta\rho & \text{for } 0 \leq z < Z_{\text{CH}_2} \cos \psi, \\ 0 & \text{for } Z_W \cos \psi \leq z \leq D/2, \end{cases} \quad (\text{B.17})$$

where $\Delta\rho = \rho_W - \rho_{\text{CH}_2}$. Then, the corresponding Fourier transform is

$$\begin{aligned} F_S &= \iint dz dx e^{iq_x x} e^{iq_z z} \rho_S(z) \delta(x \cos \psi + z \sin \psi) \\ &= \frac{2}{\cos \psi} \int_0^{Z_{\text{CH}_2} \cos \psi} dz \cos\left(\frac{\alpha}{\cos \psi} z\right) (-\Delta\rho) \\ &= -2\Delta\rho \frac{\sin(\alpha Z_{\text{CH}_2})}{\alpha}. \end{aligned} \quad (\text{B.18})$$

The bridging part of the model in the minus fluid convention is

$$\rho_B(x, z) = \frac{\Delta\rho}{2} \cos\left[\frac{-\pi}{\Delta Z_H}(z' - Z_W)\right] - \frac{\Delta\rho}{2} \quad (\text{B.19})$$

for $Z_{\text{CH}_2} \cos \psi < z < Z_W \cos \psi$, and 0 otherwise. Here, $\Delta Z_H = Z_W - Z_{\text{CH}_2}$. Then, for the strip part of the form factor, we have

$$\begin{aligned} F_B &= \iint dz dx e^{iq_x x} e^{iq_z z} \delta(x \cos \psi + z \sin \psi) \rho_B(x, z) \\ &= \frac{\Delta\rho}{\cos \psi} \int_{Z_{\text{CH}_2} \cos \psi}^{Z_W \cos \psi} dz \cos\left(\alpha \frac{z}{\cos \psi}\right) \left\{ \cos\left[-\frac{\pi}{\Delta Z_H} \left(\frac{z}{\cos \psi} - Z_W\right)\right] - 1 \right\} \\ &= \Delta\rho \left\{ \frac{\Delta Z_H \sin\left[\frac{\pi(-u+Z_W)}{\Delta Z_H} + \alpha u\right]}{-2\pi + 2\alpha \Delta Z_H} + \frac{\Delta Z_H \sin\left[\frac{\pi(u-Z_W)}{\Delta Z_H} + \alpha u\right]}{2\pi + 2\alpha \Delta Z_H} - \frac{\sin(\alpha u)}{\alpha} \right\} \Bigg|_{Z_{\text{CH}_2}}^{Z_W} \\ &= -\frac{\Delta\rho}{\alpha} [\sin(\alpha Z_W) - \sin(\alpha Z_{\text{CH}_2})] \\ &\quad + \frac{\Delta\rho}{2} \left(\frac{1}{\alpha + \frac{\pi}{\Delta Z_H}} + \frac{1}{\alpha - \frac{\pi}{\Delta Z_H}} \right) [\sin(\alpha Z_W) + \sin(\alpha Z_{\text{CH}_2})]. \end{aligned} \quad (\text{B.20})$$

Because our X-ray scattering intensity was measured in a relative scale, an overall scaling factor was necessary for a non linear least square fitting procedure. This means that $\Delta\rho$ can be absorbed in the scaling factor. Doing so means that the values of ρ_{Hi} and ρ_{M} resulting from a fitting procedure are relative to $\Delta\rho$. One way to have these parameters in the absolute scale is to integrate the bilayer electron density over

the lipid volume and equate the result to the total number of electrons in the lipid, which can easily be calculated from the chemical formula. For the ripple phase study in this thesis, the absolute values of the electron density were not of importance, so the discussion was omitted in the main text.

B.4 Correction due to refractive index

q_z needs be corrected for index of refraction. This section is practically the same as an appendix in Yufeng Liu's thesis. I include this section for mere convenience.

Let θ' and λ' be the true scattering angle and wavelength within the sample. The wavelength by an energy analyzer, λ , and the scattering angle calculated from a position on a CCD detector, θ are apparent. The correction is not necessary in the horizontal direction. The Snell's law in Fig. X gives

$$n \cos \theta = n' \cos \theta' \quad (\text{B.21})$$

$$n\lambda = n'\lambda'. \quad (\text{B.22})$$

For low angle X-ray scattering, the momentum transfer along z direction is

$$q_z = \frac{4\pi \sin \theta'}{\lambda'} \quad (\text{B.23})$$

$$= \frac{4\pi n'}{n\lambda} \sin \theta' \quad (\text{B.24})$$

$$= \frac{4\pi n'}{n\lambda} \sqrt{1 - \cos^2 \theta'} \quad (\text{B.25})$$

$$= \frac{4\pi n'}{n\lambda} \sqrt{1 - \left(\frac{n}{n'} \cos \theta\right)^2}. \quad (\text{B.26})$$

The apparent scattering angle, θ , is directly related to the vertical pixel position, p_z , by

$$\theta = \frac{1}{2} \tan^{-1} \left(\frac{p_z}{S} \right), \quad (\text{B.27})$$

where S is the sample-to-detector distance. The typical units of S and p_z are in mm. In our experimental setup, $n = 1$ and $n' = 0.9999978$ for lipids at $\lambda = 1.18 \text{ \AA}$.

Bibliography

- [1] Daniel C. Wack and Watt W. Webb. Synchrotron x-ray study of the modulated lamellar phase $p\beta'$ in the lecithin-water system. *Phys. Rev. A*, 40:2712–2730, Sep 1989.
- [2] Rainer Fischer, Mariola Fotin-Mleczek, Hansjrg Hufnagel, and Roland Brock. Break on through to the other side: biophysics and cell biology shed light on cell-penetrating peptides. *ChemBioChem*, 6(12):2126–2142, 2005.
- [3] Alain Joliot and Alain Prochiantz. Transduction peptides: from technology to physiology. *Nat Cell Biol*, 6(3), 2004.
- [4] Maria Lindgren, Mattias Hillbrink, Alain Prochiantz, and Jo Langel. Cell-penetrating peptides. *Trends in Pharmacological Sciences*, 21(3):99 – 103, 2000.
- [5] Alan D. Frankel and Carl O. Pabo. Cellular uptake of the tat protein from human immunodeficiency virus. *Cell*, 55(6):1189 – 1193, 1988.
- [6] Maurice Green and Paul M. Loewenstein. Autonomous functional domains of chemically synthesized human immunodeficiency virus tat trans-activator protein. *Cell*, 55(6):1179 – 1188, 1988.
- [7] Eric Vivas, Priscille Brodin, and Bernard Lebleu. Hiv-1 tat protein basic domain rapidly translocates through the plasma membrane and accumulates in the cell nucleus. *Journal of Biological Chemistry*, 272(25):16010–16017, 1997.
- [8] Gohar Ter-Avetisyan, Gisela Tnnemann, Danny Nowak, Matthias Nitschke, Andreas Herrmann, Marek Drab, and M. Cristina Cardoso. Cell entry of arginine-rich peptides is independent of endocytosis. *Journal of Biological Chemistry*, 284(6):3370–3378, 2009.

- [9] Gisela Tnnemann, Robert M. Martin, Simone Haupt, Christoph Patsch, Frank Edenhofer, and M. Cristina Cardoso. Cargo-dependent mode of uptake and bioavailability of tat-containing proteins and peptides in living cells. *The FASEB Journal*, 20(11):1775–1784, 2006.
- [10] Andr Ziegler, Pierluigi Nervi, Markus Drrenberger, and Joachim Seelig. The cationic cell-penetrating peptide cpptat derived from the hiv-1 protein tat is rapidly transported into living fibroblasts: optical, biophysical, and metabolic evidence. *Biochemistry*, 44(1):138–148, 2005. PMID: 15628854.
- [11] J. S. Wadia, R. V. Stan, and S. F. Dowdy. Transducible tat-ha fusogenic peptide enhances escape of tat-fusion proteins after lipid raft macropinocytosis. *Nature Medicine*, 10(3):310–315, 2004.
- [12] I. M. Kaplan, J. S. Wadia, and S. F. Dowdy. Cationic tat peptide transduction domain enters cells by macropinocytosis. *Journal of Controlled Release*, 102(1):247–253, 2005.
- [13] David A Mann and Alan D Frankel. Endocytosis and targeting of exogenous hiv-1 tat protein. *The EMBO journal*, 10(7):1733, 1991.
- [14] Jean Philippe Richard, Kamran Melikov, Hilary Brooks, Paul Prevot, Bernard Lebleu, and Leonid V Chernomordik. Cellular uptake of unconjugated tat peptide involves clathrin-dependent endocytosis and heparan sulfate receptors. *Journal of Biological Chemistry*, 280(15):15300–15306, 2005.
- [15] Simon W Jones, Richard Christison, Ken Bundell, Catherine J Voyce, Sarah Brockbank, Peter Newham, and Mark A Lindsay. Characterisation of cell-penetrating peptide-mediated peptide delivery. *British journal of pharmacology*, 145(8):1093–1102, 2005.
- [16] Agnès Vendeville, Fabienne Rayne, Anne Bonhoure, Nadir Bettache, Philippe Montcourrier, and Bruno Beaumelle. Hiv-1 tat enters t cells using coated pits before translocating from acidified endosomes and eliciting biological responses. *Molecular biology of the cell*, 15(5):2347–2360, 2004.
- [17] Christina Foerg, Urs Ziegler, Jimena Fernandez-Carneado, Ernest Giralt, Robert Rennert, Annette G Beck-Sickinger, and Hans P Merkle. Decoding the entry of

- two novel cell-penetrating peptides in hela cells: lipid raft-mediated endocytosis and endosomal escape. *Biochemistry*, 44(1):72–81, 2005.
- [18] Antonio Fittipaldi and Mauro Giacca. Transcellular protein transduction using the tat protein of hiv-1. *Advanced drug delivery reviews*, 57(4):597–608, 2005.
- [19] Ying Liu, Melina Jones, Cynthia M Hingtgen, Guojun Bu, Nick Laribee, Rudolph E Tanzi, Robert D Moir, Avindra Nath, and Johnny J He. Uptake of hiv-1 tat protein mediated by low-density lipoprotein receptor-related protein disrupts the neuronal metabolic balance of the receptor ligands. *Nature medicine*, 6(12):1380–1387, 2000.
- [20] Vladimir P Torchilin, Ram Rammohan, Volkmar Weissig, and Tatyana S Levchenko. Tat peptide on the surface of liposomes affords their efficient intracellular delivery even at low temperature and in the presence of metabolic inhibitors. *Proceedings of the National Academy of Sciences*, 98(15):8786–8791, 2001.
- [21] Vladimir P Torchilin, Tatyana S Levchenko, Ram Rammohan, Natalia Volodina, Brigitte Papahadjopoulos-Sternberg, and Gerard GM D’Souza. Cell transfection in vitro and in vivo with nontoxic tat peptide-liposome-dna complexes. *Proceedings of the National Academy of Sciences*, 100(4):1972–1977, 2003.
- [22] Carsten Rudolph, Christian Plank, James Lausier, Ulrike Schillinger, Rainer H Müller, and Joseph Rosenecker. Oligomers of the arginine-rich motif of the hiv-1 tat protein are capable of transferring plasmid dna into cells. *Journal of Biological Chemistry*, 278(13):11411–11418, 2003.
- [23] Ashok Chauhan, Akshay Tikoo, Arvinder K Kapur, and Mahavir Singh. The taming of the cell penetrating domain of the hiv tat: myths and realities. *Journal of Controlled Release*, 117(2):148–162, 2007.
- [24] JM Sabatier, E Vives, K Mabrouk, ABDELAZIZ Benjouad, H Rochat, A Duval, B Hue, and ELMOSTAFA Bahraoui. Evidence for neurotoxic activity of tat from human immunodeficiency virus type 1. *Journal of virology*, 65(2):961–967, 1991.
- [25] A. Mishra, V. D. Gordon, L. H. Yang, R. Coridan, and G. C. L. Wong. Hiv tat forms pores in membranes by inducing saddle-splay curvature: Potential

- role of bidentate hydrogen bonding. *Angewandte Chemie-International Edition*, 47(16):2986–2989, 2008.
- [26] S. T. Yang, E. Zaitseva, L. V. Chernomordik, and K. Melikov. Cell-penetrating peptide induces leaky fusion of liposomes containing late endosome-specific anionic lipid. *Biophysical Journal*, 99(8):2525–2533, 2010.
- [27] P. E. G. Thoren, D. Persson, E. K. Esbjorner, M. Goksor, P. Lincoln, and B. Norden. Membrane binding and translocation of cell-penetrating peptides. *Biochemistry*, 43(12):3471–3489, 2004.
- [28] SD Krämer and H Wunderli-Allenspach. No entry for tat (44–57) into liposomes and intact mdck cells: novel approach to study membrane permeation of cell-penetrating peptides. *Biochimica et Biophysica Acta (BBA)-Biomembranes*, 1609(2):161–169, 2003.
- [29] C. Ciobanasu, J. P. Siebrasse, and U. Kubitscheck. Cell-penetrating hiv1 tat peptides can generate pores in model membranes. *Biophysical Journal*, 99(1):153–62, 2010.
- [30] Philip A Gurnev, Sung-Tae Yang, Kamran C Melikov, Leonid V Chernomordik, and Sergey M Bezrukov. Cationic cell-penetrating peptide binds to planar lipid bilayers containing negatively charged lipids but does not induce conductive pores. *Biophysical journal*, 104(9):1933–1939, 2013.
- [31] H. D. Herce, A. E. Garcia, J. Litt, R. S. Kane, P. Martin, N. Enrique, A. Rebolledo, and V. Milesi. Arginine-rich peptides destabilize the plasma membrane, consistent with a pore formation translocation mechanism of cell-penetrating peptides. *Biophysical Journal*, 97(7):1917–1925, 2009.
- [32] Y. C. Su, A. J. Waring, P. Ruchala, and M. Hong. Membrane-bound dynamic structure of an arginine-rich cell-penetrating peptide, the protein transduction domain of hiv tat, from solid-state nmr. *Biochemistry*, 49(29):6009–6020, 2010.
- [33] S. Shojania and J. D. O’Neil. Hiv-1 tat is a natively unfolded protein - the solution conformation and dynamics of reduced hiv-1 tat-(1-72) by nmr spectroscopy. *Journal of Biological Chemistry*, 281(13):8347–8356, 2006.

- [34] P. Bayer, M. Kraft, A. Ejchart, M. Westendorp, R. Frank, and P. Rosch. Structural studies of hiv-1 tat protein. *Journal of Molecular Biology*, 247(4):529–535, 1995.
- [35] H. D. Herce and A. E. Garcia. Molecular dynamics simulations suggest a mechanism for translocation of the hiv-1 tat peptide across lipid membranes. *Proceedings of the National Academy of Sciences of the United States of America*, 104(52):20805–20810, 2007.
- [36] S. Yesylevskyy, S. J. Marrink, and A. E. Mark. Alternative mechanisms for the interaction of the cell-penetrating peptides penetratin and the tat peptide with lipid bilayers. *Biophysical Journal*, 97(1):40–49, 2009.
- [37] Y. Lyatskaya, Y. F. Liu, S. Tristram-Nagle, J. Katsaras, and J. F. Nagle. Method for obtaining structure and interactions from oriented lipid bilayers. *Physical Review E*, 63(1):0119071–0119079, 2001.
- [38] Y. F. Liu and J. F. Nagle. Diffuse scattering provides material parameters and electron density profiles of biomembranes. *Physical Review E*, 69(4):040901–040904(R), 2004.
- [39] Yufeng Liu. *NEW METHOD TO OBTAIN STRUCTURE OF BIOMEMBRANES USING DIFFUSE -RAY SCATTERING: APPLICATION TO FLUID PHASE DOPC LIPID BILAYERS*. PhD thesis, Carnegie Mellon University, 2003.
- [40] John F Nagle and Stephanie Tristram-Nagle. Structure of lipid bilayers. *Biochimica et Biophysica Acta (BBA)-Reviews on Biomembranes*, 1469(3):159–195, 2000.
- [41] Norbert Kuerka, John F. Nagle, Jonathan N. Sachs, Scott E. Feller, Jeremy Pencer, Andrew Jackson, and John Katsaras. Lipid bilayer structure determined by the simultaneous analysis of neutron and x-ray scattering data. *Biophysical Journal*, 95(5):2356 – 2367, 2008.
- [42] Stephanie Tristram-Nagle, Yufeng Liu, Justin Legleiter, and John F. Nagle. Structure of gel phase DMPC determined by x-ray diffraction. *Biophysical Journal*, 83(6):3324 – 3335, 2002.

- [43] Anthony R. Braun, Jonathan N. Sachs, and John F. Nagle. Comparing simulations of lipid bilayers to scattering data: The gromos 43a1-s3 force field. *The Journal of Physical Chemistry B*, 117(17):5065–5072, 2013.
- [44] <http://seal.web.cern.ch/seal/documents/minuit/mnusersguide.pdf>.
- [45] <http://lcgapp.cern.ch/project/cls/work-packages/mathlibs/minuit/index.html>.
- [46] Berk Hess, Carsten Kutzner, David van der Spoel, and Erik Lindahl. Gromacs 4: Algorithms for highly efficient, load-balanced, and scalable molecular simulation. *Journal of Chemical Theory and Computation*, 4(3):435–447, 2008.
- [47] Joakim P. M. Jmbeck and Alexander P. Lyubartsev. Derivation and systematic validation of a refined all-atom force field for phosphatidylcholine lipids. *The Journal of Physical Chemistry B*, 116(10):3164–3179, 2012.
- [48] Joakim P. M. Jmbeck and Alexander P. Lyubartsev. An extension and further validation of an all-atomistic force field for biological membranes. *Journal of Chemical Theory and Computation*, 8(8):2938–2948, 2012.
- [49] Viktor Hornak, Robert Abel, Asim Okur, Bentley Strockbine, Adrian Roitberg, and Carlos Simmerling. Comparison of multiple amber force fields and development of improved protein backbone parameters. *Proteins: Structure, Function, and Bioinformatics*, 65(3):712–725, 2006.
- [50] W. L. Jorgensen, J. Chandrasekhar, J. D. Madura, R. W. Impey, and M. L. Klein. Comparison of simple potential functions for simulating liquid water. *Journal of Chemical Physics*, 79(2):926–935, 1983.
- [51] Norbert Kuerka, John Katsaras, and JohnF. Nagle. Comparing membrane simulations to scattering experiments: Introducing the simtoexp software. *Journal of Membrane Biology*, 235(1):43–50, 2010.
- [52] Shuichi Miyamoto and Peter A Kollman. Settle: an analytical version of the shake and rattle algorithm for rigid water models. *Journal of computational chemistry*, 13(8):952–962, 1992.

- [53] B. Hess, H. Bekker, H. J. C. Berendsen, and J. G. E. M. Fraaije. Lincs: A linear constraint solver for molecular simulations. *J Comput Chem*, 18(12):1463–1472, 1997.
- [54] Tom Darden, Darrin York, and Lee Pedersen. Particle mesh ewald: An $n \log(n)$ method for ewald sums in large systems. *The Journal of chemical physics*, 98(12):10089–10092, 1993.
- [55] Giovanni Bussi, Davide Donadio, and Michele Parrinello. Canonical sampling through velocity rescaling. *The Journal of chemical physics*, 126(1):014101, 2007.
- [56] Michele Parrinello and Aneesur Rahman. Polymorphic transitions in single crystals: A new molecular dynamics method. *Journal of Applied physics*, 52(12):7182–7190, 1981.
- [57] Norbert Kučerka, Yufeng Liu, Nanjun Chu, Horia I Petrache, Stephanie Tristram-Nagle, and John F Nagle. Structure of fully hydrated fluid phase DMPC and DLPC lipid bilayers using X-ray scattering from oriented multilamellar arrays and from unilamellar vesicles. *Biophysical journal*, 88(4):2626–2637, 2005.
- [58] Norbert Kučerka, Stephanie Tristram-Nagle, and John F Nagle. Closer look at structure of fully hydrated fluid phase dppc bilayers. *Biophysical journal*, 90(11):L83–L85, 2006.
- [59] Norbert Kučerka, Stephanie Tristram-Nagle, and John F Nagle. Structure of fully hydrated fluid phase lipid bilayers with monounsaturated chains. *The Journal of membrane biology*, 208(3):193–202, 2005.
- [60] Stephanie Tristram-Nagle, Chao-Ping Yang, and John F Nagle. Thermodynamic studies of purple membrane. *Biochimica et Biophysica Acta (BBA)-Biomembranes*, 854(1):58–66, 1986.
- [61] <http://www.basic.northwestern.edu/biotools/proteincalc.html>.
- [62] A. C. V. Johansson and E. Lindahl. The role of lipid composition for insertion and stabilization of amino acids in membranes. *Journal of Chemical Physics*, 130(18), 2009.

- [63] S. Tristram-Nagle and J. F. Nagle. Hiv-1 fusion peptide decreases bending energy and promotes curved fusion intermediates. *Biophysical Journal*, 93(6):2048–2055, 2007.
- [64] L. B. Li, I. Vorobyov, and T. W. Allen. Potential of mean force and pk(a) profile calculation for a lipid membrane-exposed arginine side chain. *Journal of Physical Chemistry B*, 112(32):9574–9587, 2008.
- [65] I. Vorobyov, L. B. Li, and T. W. Allen. Assessing atomistic and coarse-grained force fields for protein-lipid interactions: The formidable challenge of an ionizable side chain in a membrane. *Journal of Physical Chemistry B*, 112(32):9588–9602, 2008.
- [66] J. L. MacCallum, W. F. D. Bennett, and D. P. Tieleman. Distribution of amino acids in a lipid bilayer from computer simulations. *Biophysical Journal*, 94(9):3393–3404, 2008.
- [67] E. V. Schow, J. A. Freites, P. Cheng, A. Bernsel, G. von Heijne, S. H. White, and D. J. Tobias. Arginine in membranes: The connection between molecular dynamics simulations and translocon-mediated insertion experiments. *Journal of Membrane Biology*, 239(1-2):35–48, 2011.
- [68] W. C. Wimley, T. P. Creamer, and S. H. White. Solvation energies of amino acid side chains and backbone in a family of host-guest pentapeptides. *Biochemistry*, 35(16):5109–5124, 1996.
- [69] W. C. Wimley and S. H. White. Experimentally determined hydrophobicity scale for proteins at membrane interfaces. *Nature Structural Biology*, 3(10):842–848, 1996.
- [70] B. Roux. Lonely arginine seeks friendly environment. *Journal of General Physiology*, 130(2):233–236, 2007.
- [71] W. Kabsch and C. Sander. Dictionary of protein secondary structure: pattern recognition of hydrogen-bonded and geometrical features. *Biopolymers*, 22(12):2577–637, 1983.
- [72] D. Choi, J. H. Moon, H. Kim, B. J. Sung, M. W. Kim, G. Y. Tae, S. K. Satija, B. Akgun, C. J. Yu, H. W. Lee, D. R. Lee, J. M. Henderson, J. W. Kwong,

- K. L. Lam, K. Y. C. Lee, and K. Shin. Insertion mechanism of cell-penetrating peptides into supported phospholipid membranes revealed by x-ray and neutron reflection. *Soft Matter*, 8(32):8294–8297, 2012.
- [73] K. Huang and A. E. Garcia. Free energy of translocating an arginine-rich cell-penetrating peptide across a lipid bilayer suggests pore formation. *Biophysical Journal*, 104(2):412–420, 2013.
- [74] JA Zasadzinski, J Schneir, J Gurley, V Elings, and PK Hansma. Scanning tunneling microscopy of freeze-fracture replicas of biomembranes. *Science*, 239(4843):1013–1015, 1988.
- [75] W J Sun, S Tristram-Nagle, R M Suter, and J F Nagle. Structure of the ripple phase in lecithin bilayers. *Proceedings of the National Academy of Sciences*, 93(14):7008–7012, 1996.
- [76] M. P. Hentschel and F. Rustichelli. Structure of the ripple phase P'_β in hydrated phosphatidylcholine multimembranes. *Phys. Rev. Lett.*, 66:903–906, Feb 1991.
- [77] Alex H. de Vries, Serge Yefimov, Alan E. Mark, and Siewert J. Marrink. Molecular structure of the lecithin ripple phase. *Proceedings of the National Academy of Sciences of the United States of America*, 102(15):5392–5396, 2005.
- [78] S. A. Tristram-Nagle. Preparation of oriented, fully hydrated lipid samples for structure determination using x-ray scattering. *Methods Mol Biol*, 400:63–75, 2007.
- [79] http://henke.lbl.gov/optical_constants.
- [80] M.C. Wiener, R.M. Suter, and J.F. Nagle. Structure of the fully hydrated gel phase of dipalmitoylphosphatidylcholine. *Biophysical Journal*, 55(2):315 – 325, 1989.